Pressure–temperature–deformation paths of closely associated ultra-high-pressure (diamond-bearing) crustal and mantle rocks of the Kimi complex: implications for the tectonic history of the Rhodope Mountains, northern Greece

E. Mposkos and A. Krohe

Abstract: The ultra-high-pressure (UHP) Kimi complex (uppermost eastern Rhodope Mountains) is a tectonic mixture of crustal and mantle derived associations. Pressure–temperature (P–T) paths and microtextural and geochronological data reveal that crustal and mantle parts juxtaposed against each other at a depth corresponding to ~15 kbar (1 kbar = 100 MPa) had separate ascend histories. The crustal rocks comprise amphibolitised eclogites, orthogneisses, marbles, and migmatitic pelitic gneisses. The latter document UHP metamorphism within the dehydration-melting range of pelitic gneisses, with maximum P–T conditions of >45 kbar at ~1000 °C, as determined by diamond inclusions in garnet and rutile needle exsolutions in Na-bearing garnet. Decompression was combined with only little cooling before 15 kbar, followed by more significant cooling between 15 and 10 kbar. This P–T path probably reflects ascent of UHP rocks within a subduction channel, followed by accretion in the lower crust of a thickened wedge. Although the first ascend phase was probably rapid, the overall time span for UHP metamorphism and final exhumation may have extended over more than 70 Ma. A U–Pb sensitive high-resolution ion microprobe (SHRIMP) age on zircons of ±149 Ma was suggested to date the UHP metamorphism, whereas Rb–Sr white mica and U–Pb zircon ages from syn-shearing pegmatites of ±65 Ma constrain medium- to low-grade shearing and final exhumation of UHP rocks. Mantle parts consisting of spinel–garnet metaperidotites and garnet pyroxenites reached maximum P–T conditions in the garnet-peridotite field at $T > 1200$ °C and $P > 25$ kbar. This was associated with plastic flow and followed by severe near isothermal cooling to $T < 800$ °C at 15 kbar and static annealing. A garnet–clinopyroxene whole-rock Sm–Nd age from a garnet pyroxenite of ±119 Ma probably reflects the age of metamorphic mantle processes (static annealing following the high P/high T strain episode), rather than constraining the age of UHP metamorphism.

Résumé : Le complexe de Kimi (dans la plus haute partie des monts Rhodope orientaux), est un mélange tectonique, à pression très élevée, d'associations dérivées de la croûte et du manteau. Les courbes de température et de pression et les données géochronologiques et de microtexture montrent que les parties crustales et mantelliques se sont accolées les unes aux autres à une profondeur correspondant à ~15 kbar (1 kbar = 100 MPa) et qu'elles avaient antérieurement des historiques de montée individuelle. Les roches de la croûte comprennent des éclogites amphibolitisées, des orthogneiss, des marbres et des gneiss migmatitiques pélitiques. Ces derniers reflètent un métamorphisme à très haute pression à l'intérieur de la plage de fusion de déshydratation des gneiss pélitiques avec des températures et des pressions maximales d'environ 1000 °C et >45 kbar en présentant des inclusions de diamants dans le grenat et des exsolutions d'aiguilles de rutile dans le grenat contenant du Na. La décompression a été combinée à seulement un peu de refroidissement avant d'atteindre 15 kbar; elle a été suivie d'un refroidissement plus important entre 15 et 10 kbar. Cette courbe de température et de pression est probablement le reflet de la remontée des roches à pression très élevée dans un chenal de subduction, suivie de l'accrétion d'un coin épaissi au niveau de la croûte inférieure. Bien que la première phase de la remontée ait probablement été rapide, l'intervalle de temps global entre le métamorphisme à pression très élevée et l'exhumation finale peut s'étendre sur plus de 70 Ma. Un âge de ±149 Ma, par détermination U–Pb sur une microsonde à haute résolution et à haut niveau de sensibilité (SHRIMP) sur des zircons, est suggéré pour dater le métamorphisme à très haute pression alors que les âges Rb–Sr déterminés sur des micas blancs et les âges U–Pb sur des pegmatites à

E. Mposkos. National Technical University of Athens, School of Mining and Metallurgical Engineering, Section of Geological Sciences, 9 Heroon Polytechniou Str., Gr-15780 Zografou Athens, Greece.
A. Krohe.[1] University of Muenster, Institute for Mineralogy, Laboratory for Geochronology, Corrensstrasse 24, D-48149 Muenster, Germany.

[1]Corresponding author (e-mail: krohe@nwz.uni-muenster.de).

doi:10.1139/E06-064

cisaillement synchrone de ±65 Ma limitent le cisaillement moyen à faible et l'exhumation finale des roches à très haute pression. Les parties du manteau composées de métapéridotites à grenat et spinelle et des pyroxénites à grenat ont connu des conditions de pression et de températures maximales dans le champ péridotite à grenat, à $T > 1200$ °C et $P > 25$ kbar. Ces conditions étaient associées à un écoulement plastique suivi d'un refroidissement isotherme abrupt à $T < 800$ °C et à $P = 15$ kbar accompagné d'une recuisson statique. Déterminé par Sm–Nd à partir d'une pyroxénite, l'âge de ±119 Ma pour la roche entière, un clinopyroxène à grenat, reflète probablement l'âge du processus de métamorphisme du manteau (recuisson statique après l'épisode de contraintes à haute pression / haute température), plutôt que de limiter l'âge du métamorphisme à très haute pression.

[Traduit par la Rédaction]

Introduction

Ultra-high-pressure (UHP) rocks are commonly associated with rocks that do not seem to have undergone such high pressures. This is either because equilibration phases during ascent have masked the petrological record of peak pressure–temperature (P–T) conditions, or because the P–T paths differ through different parts of the UHP complex. Therefore, detailed petrological investigations of different lithologies of UHP complexes, integrated with fabric analyses and geochronological data, are necessary to illuminate the following essential issues.

(1) Are UHP complexes subducted into and exhumed from the mantle as coherent blocks as was suggested, for example, for the Dabie UHP metamorphic complex (e.g., Rolfo et al. 2003)? This would result in a homogeneous P–T history through the entire UHP complex. Or do tectonic processes during ascent juxtapose UHP rocks against lower P rocks and mantle material that does not show UHP metamorphism? This has been described for the Paleozoic Erzgebirge composite UHP complex (Massonne 1999, 2005; Massonne and O'Brien 2003; Willner et al. 2002).

(2) Do UHP metamorphic complexes generally show more or less single phase and rapid ascent histories, as has been suggested for most presently known UHP complexes, or could ascent of UHP rocks also be more prolonged with a polyphase tectonic history?

The Kimi UHP metamorphic complex in the Alpine Rhodope, in the north-eastern Hellenic orogen (Fig. 1; Krohe and Mposkos 2002), is one of the very few occurrences of diamond-bearing SiO_2-rich rocks (Mposkos and Kostopoulos 2001; Perraki et al. 2006), which are typically found in continental crust; these rocks are referred to in the following text as diamond-bearing migmatized metapelites. Associated crustal rocks are marbles and meta-igneous rocks (amphibolites, eclogite amphibolites, granitic to dioritic orthogneisses) that are intimately associated with mantle-derived spinel–garnet metaperidotites and garnet pyroxenites. Widespread muscovite pegmatites crosscut through all lithological assemblages. So far UHP metamorphism has been unambiguously proven to occur only in the diamond-bearing migmatitic pelitic gneisses.

This article presents P–T paths and fabric data from metapelites and metaperidotites. Integrating petrological and tectonic aspects of the crustal assemblage and the mantle rocks provides important insights into the understanding of mass transfer through the Earth's interior that causes recycling and reprocessing of the crust and has important implications

for geotectonic evolution of the Alpine Rhodope domain. We show that UHP metamorphic crustal and mantle rocks of the Kimi complex have different, probably unrelated, early P–T histories and were juxtaposed against each other during ascent in the lithosphere at a depth of ca. 40–50 km. This precludes crustal and mantle rocks from having a common subduction history or being dragged up from maximum depth by subducted continental material. We further argue that ascent of the UHP rocks was polyphase, including a prolonged annealing and recrystallization episode in the lower crust, contrasting with the Erzgebirge and Dabie UHP complexes. Overprinted crustal and mantle rocks conceal much of the early tectonometamorpic history.

Geological overview

The Rhodope high-pressure (HP) province occupies the easternmost part of the Hellenic orogen. It incorporates several tectonic slivers of reprocessed Paleozoic (Variscan) crust (Mposkos and Wawrzenitz 1995; Wawrzenitz 1997; Liati and Gebauer 1999), and probably post-Variscan oceanic and continental margin sediments (although metasediments do not preserve any paleontological age constraints). All recent geochronological and structural investigations unequivocally reveal that the Rhodope province is an Alpine synmetamorphic thrust and nappe complex (Burg et al. 1996; Dinter 1998; Ricou et al. 1998; Liati and Gebauer 1999; Lips et al. 2000; Mposkos and Krohe 2000) and rule out previous interpretations of this province as a pre-Alpine "stable" block exclusively preserving pre-Alpine metamorphism. According to Krohe and Mposkos (2002), this thrust and nappe complex formed during Cretaceous to mid-Tertiary plate convergence, material accretion, and collision between Africa and Europe. From the Late Eocene up to the Miocene, several generations of low-angle normal detachment systems developed. These formed during and after thrusting, tore apart the nappe complex, and exhumed its deeper parts (Krohe and Mposkos 2002).

Mposkos and Krohe (2000) and Krohe and Mposkos (2002) subdivided the Rhodope HP province into several tectonometamorphic units that are bounded by thrust and normal faults. These segments differ in P–T conditions during their HP metamorphism, shape of P–T paths, and timing of exhumation. In the eastern Rhodope Mountains, the Kimi complex is the uppermost structural metamorphic unit, and it was the first exhumed. It contains the diamond-bearing UHP rocks (Mposkos and Kostopoulos 2001; Perraki et al. 2006); its exhumation was between 65 and >48 Ma. The Kimi com-

Fig. 1. Geological map of central and eastern Rhodope Mountains (after Mposkos and Krohe 2000, simplified) with locations of diamond containing metapelites.
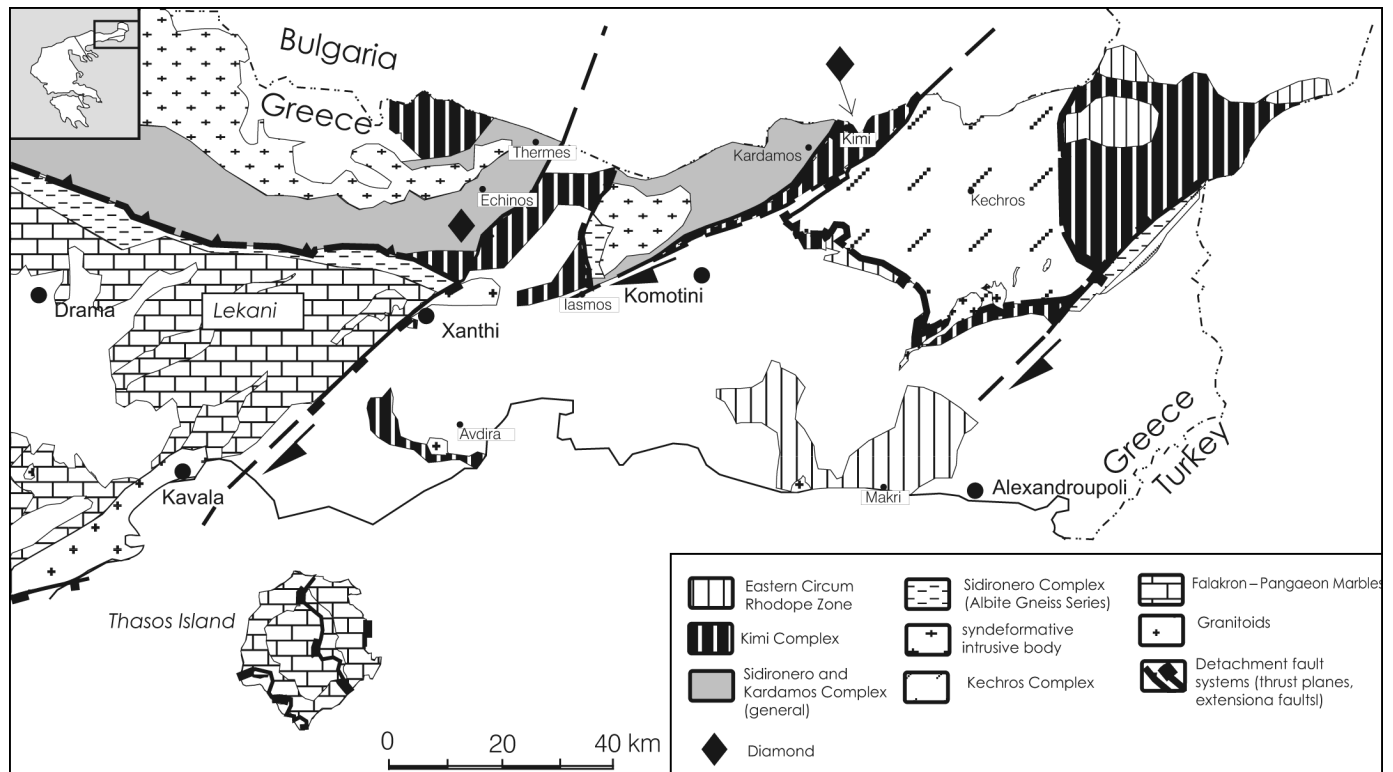
plex is only a few 100 m thick and tectonically sandwiched between tectonic blocks that record totally different metamorphic and exhumation histories. Its upper plate consists of unmetamorphosed Jurassic ophiolites and only weakly metamorphosed rocks (eastern Circum Rhodope Zone). Transgression of sediments in the Middle Eocene (Lutetian, 42–50 Ma, Harland et al. 1990) onto the Kimi complex and the eastern Circum Rhodope Zone defines the minimum age for denudation of the Kimi complex and its juxtaposition underneath the eastern Circum Rhodope Zone. By contrast, the lower plate, which is bounded to the Kimi complex by successively formed systems of low angle normal faults, shows a Late Eocene and thus distinctly younger HP metamorphism (Liati and Gebauer 1999). This lower plate is a composite thrust complex consisting of the Kardamos, Kechros (~15 kbar (1 kbar = 100 MPa) and ~550 °C, Mposkos 1989), and Sidironero sub-complexes (>19 kbar at 700 °C; Liati and Seidel 1996). The lowermost tectonometamorphic complex of the Rhodope province is the Miocene Thasos–Pangeon metamorphic core complex (Sokoutis et al. 1993; Dinter et al. 1995; Wawrzenitz and Krohe 1998).

In the following, we discuss the peak *P–T* conditions and the shape of the decompression *P–T* paths of the diamond-bearing metapelites and the mantle assemblage, as well as their implications for the tectonic processes of the Kimi complex. For this purpose, we present new petrological and textural data from diamondiferous kyanite-bearing migmatitic metapelites, spinel–garnet metaperidotites, and garnet pyroxenites.

High-alumina diamond-bearing migmatitic pelitic gneisses

Mineral assemblage

UHP metasediments that bear diamonds are migmatitic high-alumina metapelites including garnet–kyanite–muscovite–biotite gneisses (mineral assemblage: Grt–Ky–Bt–Ms–Pl–Kfs–Qtz–Rt ± St ± Chl, abbreviations after Kretz 1983). Accessory minerals are zircon, apatite, ilmenite, tourmaline, allanite, *diamond*, graphite, Mg-siderite, galena, and sphalerite. A bulk-rock analysis of a diamond-bearing sample yielded SiO_2, 61.48%; TiO_2, 1.1%; Al_2O_3, 17.71%; FeOt, 7.38%; MnO, 0.1%; MgO, 3.55%; CaO, 0.98%; Na_2O, 1.1%; K_2O, 2.96%; and P_2O_5, 0.1%. The rocks preserve several generations of garnet, biotite, muscovite, and kyanite. Mineral chemistry and textural relationships constrain peak pressures and retrogressive *P–T* path.

Garnet

Garnet porphyroblasts grew during UHP metamorphism and during initial decompression stages. Garnet growth at UHP conditions is indicated by diamond inclusions. Additionally, garnet contains single-grain inclusions of quartz, kyanite, rutile, biotite, zircon, graphite, allanite, and apatite, as well as polyphase inclusions of biotite + muscovite (Fig. 2A), biotite + muscovite + quartz + rutile (Fig. 2B), biotite ± muscovite + kyanite + quartz + rutile (Fig. 2C), and biotite + kyanite + plagioclase + quartz. Rational interfaces are common between garnet host and mica inclusions in

Fig. 2. Diamond-bearing metapelites. Scanning electron microscopy (SEM) photographs: (A, B) Polyphase inclusions in garnet with rational mica–garnet interfaces developed by continuous reaction between inclusion and host garnet. Photomicrographs, polarizer only: (C) Polyphase inclusions in garnet with rational mica–garnet interfaces developed by continuous reaction between inclusion and host garnet; (D) Quartz inclusions in garnet with rational interfaces crystallized from a supercritical fluid entrapped into the growing garnet at ultra-high-pressure conditions; (E) Inclusion of quartz grain (former coesite) in garnet (note the fractures that emanate from the quartz inclusion into the hosting garnet); (F) Kyanite aggregates (Ky-2) and biotite flakes grow at the expense of garnet and muscovite; (G) Kyanite aggregate replacing possible former andalusite (?). SEM photograph: (H) Granophyric intergrowths of plagioclase, quartz and kyanite in a matrix leucosome, consisting of plagioclase + quartz + kyanite (rods) + muscovite ± biotite.
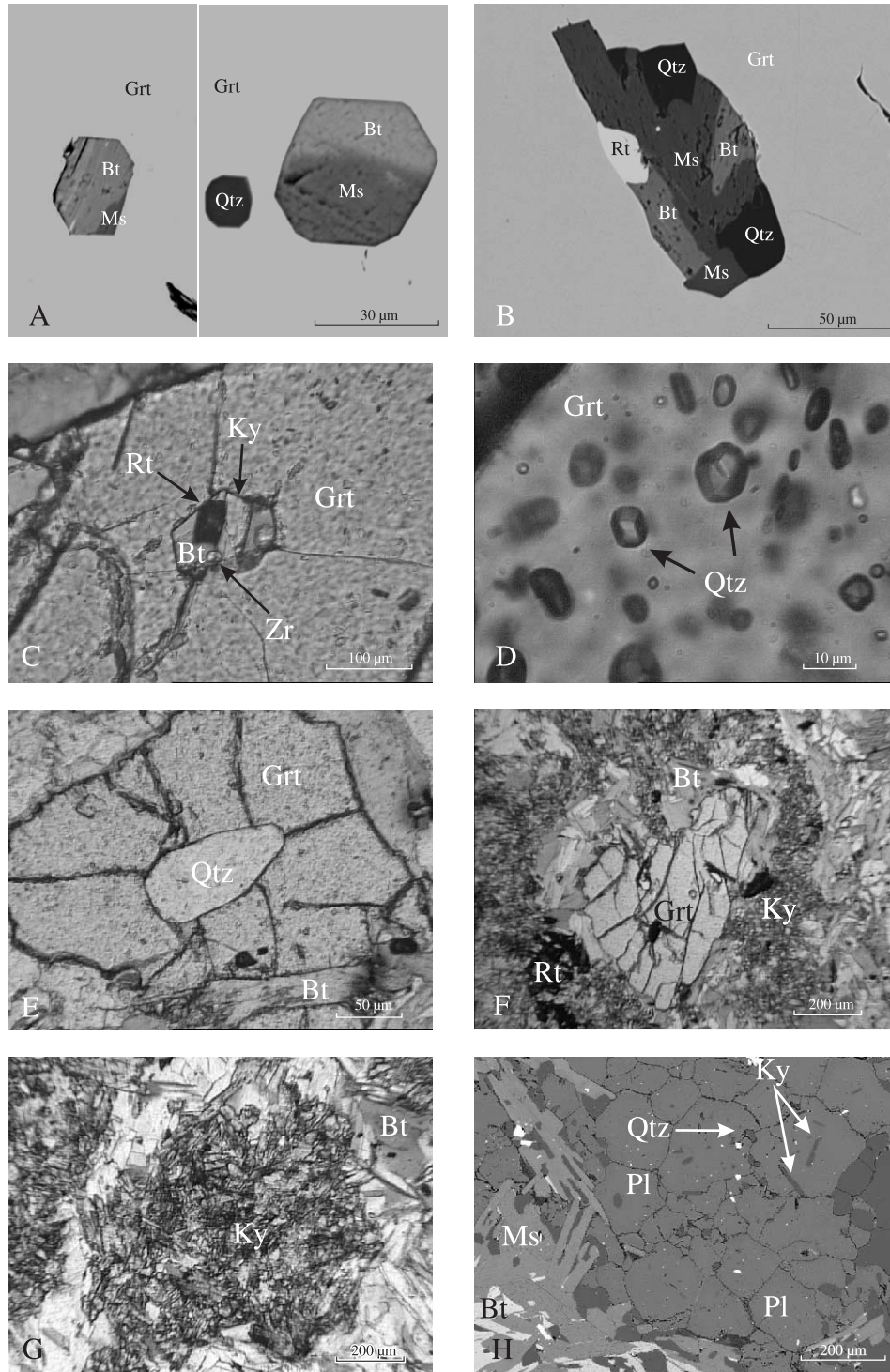
single-grain inclusions, as well as in polyphase inclusions (Figs. 2A, 2C). Polyphase inclusions in garnet with rational mica–garnet interfaces are also described by Stöckhert et al. (2001) from diamond-bearing UHP metamorphic gneisses from Erzgebirge. Stöckhert et al. (2001) interpreted such polyphase inclusions as being developed by continuous reaction between trapped supercritical fluid or melt and the host garnet. There are two types of rutile inclusions: (1) rutile grains (20–100 µm in diameter) that do not show preferred growth orientation with respect to garnet, and (2) rutile needles (<<1 µm wide, up to 100 µm long) that are characterized by preferred growth with respect to the host garnet. These have been interpreted as exsolutions from a former titaniferous garnet. There are also two types of quartz inclusions. The first consists of minute quartz grains (5–20 µm in size) with rational interfaces with the host garnet (Fig. 2D); quartz grains are commonly associated with rutile, graphite, and biotite, and may contain inclusions of rutile, graphite, zircon, and apatite. Such inclusions are interpreted as having crystallized within the stability field of quartz during decompression and cooling from a supercritical fluid that was entrapped into the growing garnet at UHP conditions (Schmickler et al. 2004). The second consists of larger quartz inclusions (30–100 µm in size), which are surrounded by fractures in the host garnet (Fig. 2E), possibly represent former coesite transformed to quartz during decompression. No coesite inclusions have been found despite our persistent searching with Raman spectroscopy. Possibly, prolonged annealing in the lower crust caused transformation of coesite to quartz and the recovery and recrystallization of fractured garnet adjacent to the inclusions (see Discussion). Garnet shows resorbed edges and is usually replaced by biotite, biotite + kyanite (Fig. 2F), and plagioclase during decompression and cooling.

Kyanite

Textural relationships suggest two generations of kyanite. Kyanite-1 (Ky-1) is found as porphyroblasts (up to 2 cm in size), inclusions in garnet, and aggregates of medium-grained (0.1–0.2 mm in size), sub-idiomorphic grains. Clusters of kyanite aggregates (Fig. 2G) possibly replaced former Al-silicate phases (i.e., andalusite), suggesting a polymetamorphic history for the metapelites. The second kyanite generation (Ky-2) is found as thin prisms or needles (20–100 µm in size) intergrown with biotite and replacing garnet and muscovite (Fig. 2F).

Mica

A number of textural variations of muscovite record several equilibration stages during subduction and exhumation. Large muscovite flakes (up to 500 mm) are intergrown with biotite flakes and contain exsolution needles of rutile, suggesting formation from titanium-rich phengite during decompression. Ti-rich muscovite (TiO$_2$ up to 3 wt.%, Fig. 2A; analysis 1, Table 1) associated with biotite also occurs as inclusions in garnet. Ti-rich muscovite and biotite are interpreted as formed during decompression from previous Ti-rich phengite inclusions. Similar Ti-rich phengite occurs in diamondiferous pelitic gneisses from the Kokchetav Massif (Kazakhstan) and the Saxonian Erzgebirge (Hermann et al. 2001; Massonne 1998, 2003), and it has been recognized as an UHP phase by

Hermann et al. (2001) and a HP phase by Massonne (1998, 2003). Muscovite aggregates replacing pseudomorphic kyanite porphyroblasts are Ti-poor (analysis 3, Table 1), formed by water influx during exhumation.

Abundant matrix biotite + kyanite (Ky-2) was formed during decompression, mostly at the expense of garnet (Fig. 2F), according to the water-preserving reaction: Grt + Ms → Bt + Ky + Qtz (Le Breton and Thompson 1988; Vielzeuf and Holloway 1988). As inclusions in garnet, biotite occurs as single or composite grains associated with muscovite, rutile, kyanite, plagioclase, and quartz. Where biotite and muscovite are both present, biotite generally replaces muscovite, suggesting biotite formation from former phengite inclusions that reacted with the enclosing garnet during exhumation according to the water-conserving reaction Pheg + Grt → Ms + Bt + Qtz. Green or pale brown biotite with a very low Ti-content (analysis 4, Table 1) replaces garnet and muscovite, presumably at low greenschist-facies conditions.

Feldspar

K-feldspar is rarely preserved in the matrix with corroded edges. K-feldspar is replaced by muscovite and biotite according to the reaction Grt + Kfs + W/L → Bt + Ms + Pl + Qtz. Aggregates consisting of small grains of quartz and plagioclase, interstitial flakes of muscovite and biotite, as well as of kyanite prisms and rods enclosed by plagioclase and quartz, are interpreted as neosome pockets that crystallized from a melt. Granophyric intergrowths of plagioclase and quartz (Fig. 2H) indicate simultaneous crystallization. The lack of shape-preferred orientation in all phases indicates static crystallization.

Staurolite

Retrogressive staurolite is associated with chlorite and muscovite replacing kyanite, biotite, and garnet. Staurolite shows compositional zoning with decreasing Mg/(Mg + Fe) ratio (Mg#) from the core to the rim (Table 1), indicating further growth of staurolite by the continuous hydration reaction Grt + W → St + Chl + Qtz. The Zn content in staurolite ranges from 2.21 to 2.66 wt.% ZnO.

Chlorite

Chlorite is associated with garnet, staurolite, and muscovite, replacing kyanite and probably pre-existing matrix biotite.

Pressure–temperature path of the metapelites

Peak metamorphism and first decompression episode

Inclusions of diamond cubes and octahedra (3–7 µm in size) in garnet are the most definite evidence that crustal assemblages of the Kimi complex underwent UHP conditions, exceeding 45 kbar for assumed temperature of 1000 °C (Kennedy and Kennedy 1976). Diamond exclusively occurs as inclusions in garnet porphyroblasts. In situ laser Raman spectroscopy in diamond inclusions in garnet that are not exposed to the surface yielded diagnostic spectra of pure diamonds and of partially or completely graphitized diamonds (Figs. 3A, 3B) (Mposkos et al. 2004; Perraki et al. 2004,

Table 1. Representative compositions of muscovite, biotite, staurolite, garnet, chlorite, and plagioclase from diamodiferous metapelites from the Kimi complex.

	1 Ms i-Grt	2 Bt i-Grt	3 Ms	4 Bt	5 St core	6 St rim	7 Chl	8 Grt	9 Bt-2 m	10 Grt	11 Bt-2 m	12 Grt	13 Plg	14 Grt	15 Plg
SiO_2	46.91	37.34	46.90	35.80	28.68	28.55	27.29	37.49	35.65	37.64	34.23	38.85	62.26	38.63	62.19
TiO_2	3.04	4.05	0.22	0.92	0.57	0.52	—	—	1.64	—	2.96	—	—	—	—
Al_2O_3	32.07	18.29	34.18	19.37	51.45	52.63	23.61	21.28	19.35	21.34	19.17	21.91	23.30	21.75	23.50
FeO	1.52	11.12	2.53	20.31	12.18	11.82	16.39	32.08	17.54	32.82	18.63	26.00	0.25	27.44	0.36
MnO	—	—	—	0.05	—	—	—	2.16	—	0.98	—	0.55	—	0.71	—
MgO	1.68	14.03	1.53	10.10	2.66	2.21	20.72	3.98	10.55	4.37	11.04	7.08	—	6.40	—
CaO	—	—	—	—	—	—	—	2.90	—	2.79	—	5.66	4.80	4.95	5.00
Na_2O	0.84	0.40	1.18	0.05	ZnO = 2.79	ZnO = 2.66	—	—	0.24	—	0.32	—	8.80	—	8.90
K_2O	10.00	9.90	9.58	10.12	—	—	—	—	8.61	—	9.68	—	0.26	–	0.21
Total	96.06	95.13	96.12	96.72	98.33	98.40	88.02	99.85	94.58	99.96	96.03	100.04	99.67	99.88	100.16
Si	6.215	5.475	6.208	5.401	8.15	8.081	5.422	2.995	5.419	2.995	5.168	3.002	2.771	3.008	2.759
Ti	0.303	0.447	0.022	0.104	0.12	0.110	—	—	0.187	—	0.336	—	1.222	—	—
Al	5.007	3.161	5.332	3.444	17.23	17.553	5.530	1.999	3.467	2.001	3.420	1.996	0.009	1.996	1.227
Fe	0.168	1.364	0.280	2.563	2.89	2.798	2.723	2.143	2.230	2.184	2.359	1.680	—	1.787	0.013
Mn	—	—	—	0.006	1.27	0.932	—	0.146	—	0.066	—	0.036	—	0.047	—
Mg	0.331	3.067	0.302	2.271	Zn = 0.58	Zn = 0.557	6.137	0.474	2.390	0.518	2.490	0.816	0.229	0.743	—
Ca	—	—	—	—	—	—	—	0.248	—	0.238	—	0.468	0.759	0.413	0.237
Na	0.216	0.114	0.302	0.014	—	—	—	—	0.071	—	0.093	—	0.015	—	0.765
K	1.690	1.852	1.618	1.948	—	—	—	—	1.863	—	1.870	—	—	—	0.012
Total	13.93	15.48	14.06	15.751	30.24	30.031	19.812	8.005	15.627	8.002	15.736	7.998	5.005	7.994	5.013
Mg/(Mg + Fe)		0.69		0.47	0.30	0.25	0.69		0.52		0.51				

Note: Analyses 8 to 15 are used for geothermometry and geobarometry. Ms, muscovite; Bt, biotite; St, staurolite; Chl, chlorite; Grt, garnet; Plg, plagioclase; i-Grt, inclusion in garnet; m, matrix. Grt–Bt thermometry (Ferry and Spear 1978). Pairs: 8–9 = 673 °C, 10–11 = 705 °C for 15 kbar. Garnet–plagioclase–kyanite–quartz barometry (Koziol and Newton 1988). Pairs: 12–13 = 12.66 kbar/600 °C, 14.77 kbar/700 °C. 14–15 = 12.4 kbar/600 °C, 14.47 kbar/700 °C. Numbers are cations per oxygenes (22 for Ms, Bt; 47 for St; 12 for Grt; 28 for Chl; 8 for Plg). Major oxides in wt.%.

Fig. 3. Diamond-bearing metapelites. Representative Raman spectra of (A) pure diamond and (B) partially graphitized diamond inclusions in garnet that verify undisputedly the ultra-high-pressure (UHP) metamorphism in the Kimi complex of the Rhodope metamorphic province; both the pure and partially graphitized diamond inclusions are not exposed to the garnet surface. Photomicrographs, polarizer only. (C) Oriented carbon-bearing polyphase inclusions (~4–10 μm in size) with parallel faces into the garnet host consisting of Mg-siderite ± CO_2 + diamond or graphite. (D) Oriented rutile needles and quartz rods characterized by preferred growth with respect to the host garnet, interpreted as exsolutions from a former UHP Na-bearing titaniferous garnet.
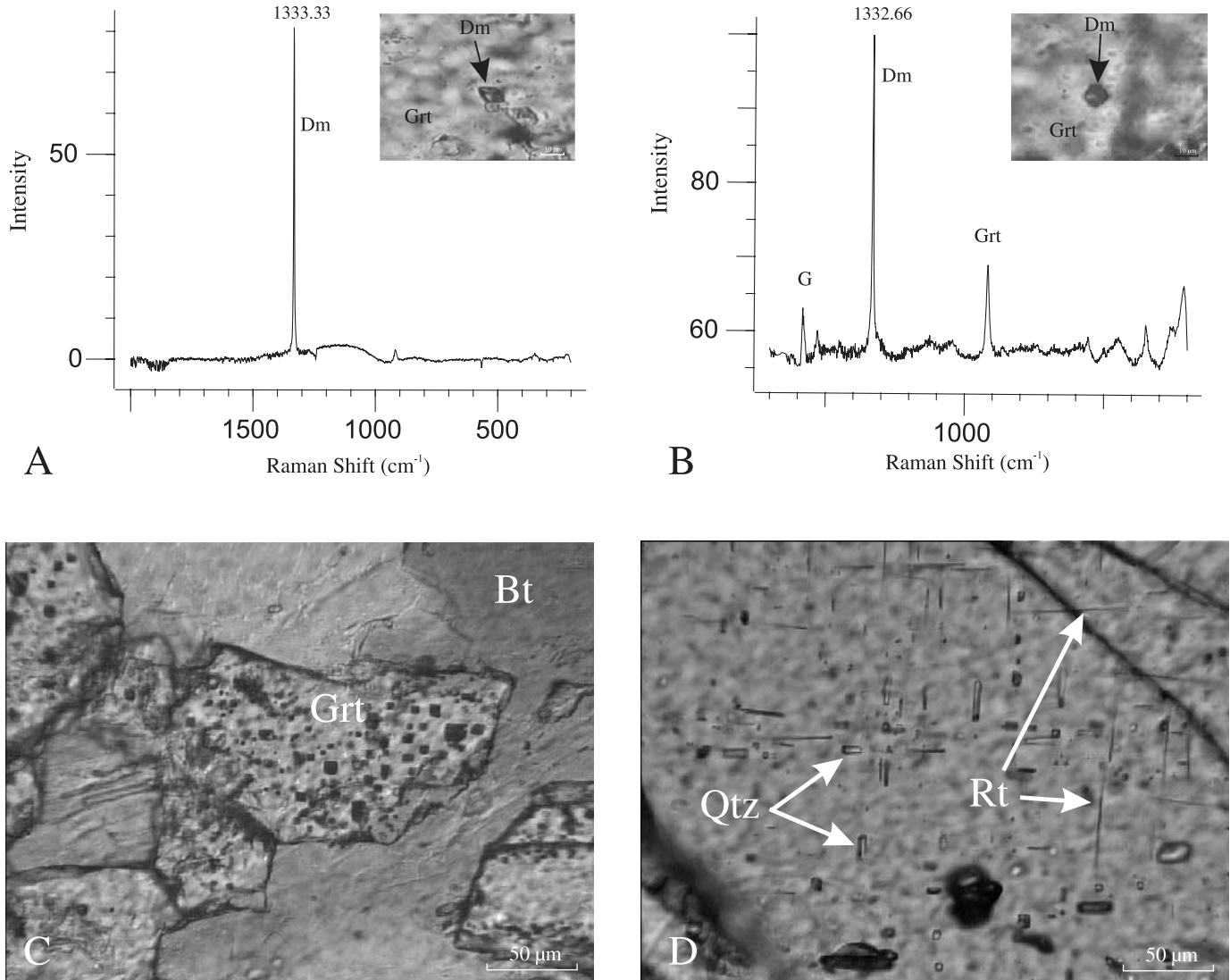
2006). The Raman microspectroscopy combined with microprobe analyses have also shown various carbon-bearing polyphase inclusions (~4–10 μm in size) that show rational interfaces with the garnet host (Mposkos and Kostopoulos 2001, figs. 2B, 3C; Perraki et al. 2006, fig. 2C) may consist of Mg-siderite ± CO_2 + diamond or graphite (Stamoudi and Mposkos 2005) with additional biotite, muscovite, quartz, rutile, zircon, and apatite.

These data suggest that diamond possible precipitated from C–O–H + silicate supercritical fluids rich in Fe, Al, Mg, K, Zr, and P entrapped within garnet that grew at UHP conditions. Experimental studies show that crystallization of diamond may occur from CO_2 or C–O–H fluid at a supercritical stage (Akaishi et al. 2000; Yamoaka et al. 2002). Crystallization of diamond from fluid inclusions in garnet

has been proposed to occur in natural UHP rocks (Stöckhert et al. 2001; Dobrzhinetskaya et al. 2003).

Typical of UHP are sodic garnets containing silica rods (<1 μm wide, ~20 μm long), apatite, and rutile needles (<<1 μm wide, up to 100 μm long) that are characterized by preferred growth with respect to the host garnet (Fig. 3D). These have been interpreted as exsolutions from a former UHP garnet phase that was richer than normal in Ti, Na, and P (Mposkos and Kostopoulos 2001).

Petrological experiments that used diamondiferous metapelites from the Kimi complex as starting material at 60 kbar and 1000 °C support these high *P–T* conditions. The experiments yielded the mineral assemblage garnet + clinopyroxene + phengite + coesite + kyanite + rutile (Konzett, personal communication, 2004) with a synthesized

garnet showing Na_2O, P_2O_5, and TiO_2 values of 0.30%, 0.25%, and 1%–2%, respectively. Other garnets synthesized in UHP experiments at 900–1000 °C, 45 kbar, by using pelitic rock compositions (Hermann, personal communication, 2005) also yielded TiO_2, 0.81%–0.90%; Na_2O, 0.37%–0.48%; and P_2O_5, 0.39%–0.47%. Such values approximate those reported by Mposkos and Kostopoulos (2001) for natural sodic garnet of the UHP metasediments. The Na_2O and P_2O_5 contents in garnet are pressure dependent (Okamoto and Maruyama 1998; Ono 1998), and the TiO_2 content is temperature dependent (Massonne 2003). Therefore, the actual chemical composition of the garnets from the diamondiferous metapelites of the Kimi complex (Na_2O = 0.60%, P_2O_5 = 0.33%, TiO_2 = 1.03%, Mposkos and Kostopoulos 2001) indicates that the diamond-bearing metapelites were likely exposed to P–T conditions reaching ~50 kbar and ~1000 °C.

At near-peak P–T conditions, or at the first stages of decompression, partial melting occurred in the metapelites as indicated by their migmatitic textures. Potassic feldspar and garnet were likely produced via dehydration melting of the metapelites as they probably crossed the reaction curve Phe + Coe + Cpx → Grt + Ky + Kfs + L (Hermann and Green 2001; reaction curve 1, Fig. 4).

This can be inferred from the chemistry of some zoned garnets. Most garnet porphyroblasts are homogeneous with only the outermost rims showing retrograde diffusion zoning with decreasing Mg and increasing Fe and Mn (Mposkos and Liati 1993, figs. 8A, 8C). However, few garnet porphyroblasts with rutile needle exsolutions that are thought to have grown at UHP conditions preserve domains of sodic garnet (Mposkos and Kostopoulos 2001, Table 2) and compositional zoning (Fig. 5) with Ca-rich and compositionally quite homogeneous cores (0.5 mm, Grt_{13} Prp_{22} Alm_{62} $Sps_{1.8}$). Zoning is characterized by continuously decreasing Ca and increasing Mg and Fe through the rim and is interpreted as an overgrown zone (0.8 mm in size). The Mn content remains constant from the core through this zone. Similar zoning patterns, i.e., Ca-decrease and Mg-increase, are shown in garnets of diamond-bearing quartzofeldspathic rocks from the Erzgebirge (Massonne 2001; Stöckhert et al. 2001). Experiments on pelitic bulk-rock composition from 20 to 45 kbar indicate that the Ca content of garnet coexisting with clinopyroxene and kyanite decreases with decreasing pressure at a constant temperature (Hermann and Green 2001). These results suggest that the Ca-rich core of these garnets may preserve the chemical composition from the UHP stage, whereas the outer zone reflects garnet growth during decompression from mantle depths to the lower crust.

Second exhumation stage: cooling combined with slow decompression

Textures, mineral assemblages, and mineral compositions of the diamondiferous metapelites indicate a second exhumation stage that is characterized by substantial cooling and slow decompression between ~16 and 12 kbar, corresponding to a depth of 43–55 km, probably at the base of a thickened crust (stage B, Fig. 4). This equilibration stage is defined in the following text.

Corroded K-feldspar rims indicate K-feldspar consump-

Fig. 4. P–T–t diagram showing the exhumation path of the diamondiferous metapelites in the ultra-high-pressure metamorphic Kimi complex (eastern Rhodope Mountains). A–C are different stages discussed in the text. 1–9 are the reaction curves.

1) Phen+Cs+Cpx → Grt+Ky+Kfs+L
2) Ms+Pl+Qtz→Als+Kfs+L
3) Bt+Als+PL+Qtz→Grt+Kfs+L
4) Bt+Ms+Pl+Qtz→Grt+Kfs+L
5) Kfs+Ab+Qtz+W→L
6) Cld→St+Chl+Qtz
7) Grt+Chl+Ms→St+Bi
8) St→Grt+Chl+Ky
9) Pl(An₁₅)+Kfs+W→Czo+Ms+Pg+Qtz
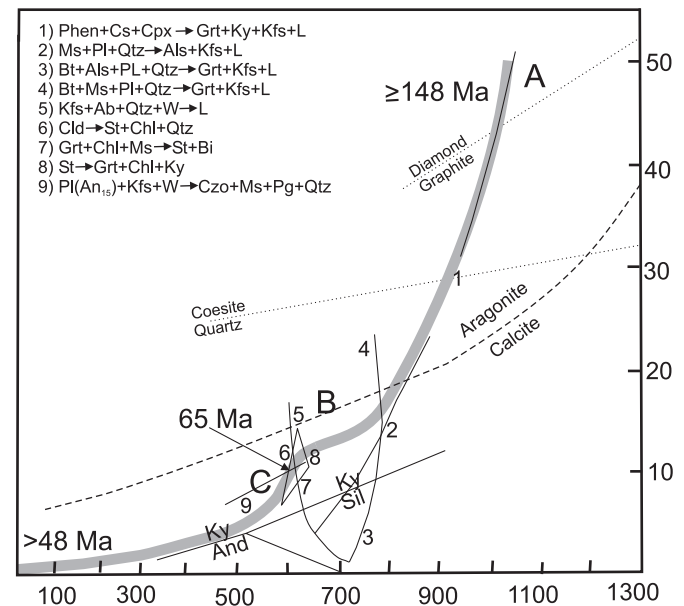
tion during melt crystallization according to the reaction Grt + Kfs + L → Bt + Ms + Pl + Qz. The resultant mineral assemblage is predominant in the matrix. According to experimental results of Le Breton and Thompson (1988) and Vielzeuf and Holloway (1988), this reaction occurs at pressures >15 kbar (reaction curve 4, Fig. 4).

Garnet and muscovite are extensively replaced by biotite and kyanite (Ky-2) (Fig. 2F), at pressure <15 kbar, according to the pressure-dependent reaction Grt + Ms + (H_2O) → Bt + Ky + Qtz (Le Breton and Thompson 1988; Vielzeuf and Holloway 1988). Cooling at this stage is recorded by the zoning at the outermost rim of the resorbed garnet edges (see garnet compositional profile in Fig 5 from this paper and figs. 8A, 8C from Mposkos and Liati 1993). Such garnets, coexisting with matrix biotite, kyanite, plagioclase, and quartz, show retrograde diffusion zoning at the outermost rim with increasing Mn and Fe (and Ca, if they are in contact with plagioclase) and decreasing Mg, characterizing a later retrogression stage. Garnet–biotite geothermometry (Ferry and Spear 1978) between garnet rim and matrix biotite in contact with the garnet yielded temperatures in a range between 600 and 700 °C (Table 1). A Ca increase in garnet toward the rim that is in contact with plagioclase, kyanite, and quartz is a characteristic feature of near-isobaric cooling from granulite facies to upper-amphibolite facies in lower crustal rocks (Hermann et al. 1997). Applying the garnet–plagioclase–kyanite–quartz geobarometer (Koziol and Newton 1988) on coexisting phases gives pressures between 12.5 and 14.5 kbar at 600–700 °C (Table 1). Lenses of dolomitic marbles within migmatitic pelitic gneisses also record minimum pressure of 17 kbar and temperature of 750 °C by the mineral assemblage Mg-calcite–dolomite–olivine–spinel ± diopside + phengite + phlogopite. Matrix Mg-calcite ($XMgCO_3$ 0.14 mol) records an equilibration temperature of 750 °C (Anovitz and Essene 1987) and

Fig. 5. Compositional zoning profile of garnet porphyroblast from a diamond-bearing metapelite showing two stages of garnet growth (see text for explanation).
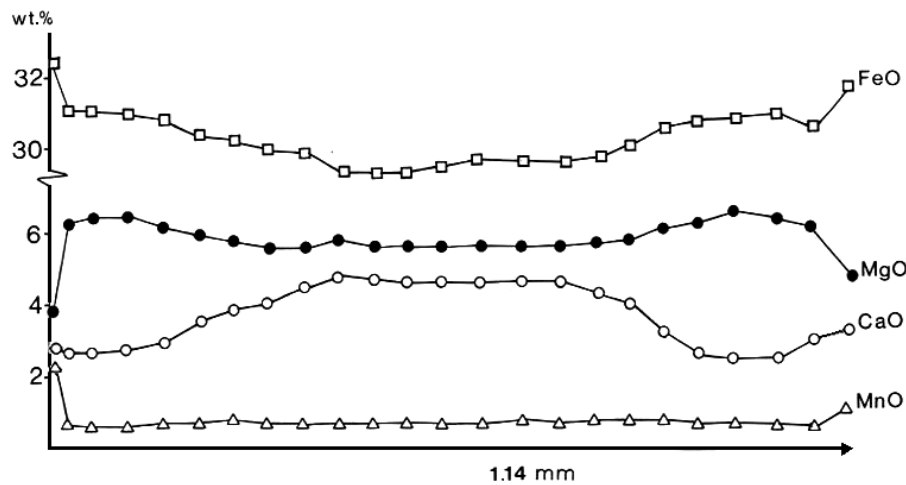
Fig. 6. Elongated mafic enclaves in a dioritic gneiss having long axis to short axis ratios of more than 20:1 define a high-pressure and high-temperature foliation and lineation. Trondhjemitic pegmatite dyke (mineral assemblage: Pl + Qtz + Czo + Ms + Pg ± Ky) intruded during the post-deformational static annealing and reequilibration stage cuts across the foliation.

phengite (Si = 3.5 atoms per formula unit) a minimum pressure of 17 kbar (Massonne and Szpurka 1997) at this exhumation stage. Dolomite exsolutions in Mg-calcite ($X\mathrm{MgCO_3}$, 0.058–0.075 mol) occurred at 550–610 °C.

The crosscutting muscovite pegmatites (Fig. 6) showing the mineral assemblage plagioclase ($\mathrm{An_{15–20}}$) + muscovite + clinozoisite + quartz ± paragonite also record cooling at depth. The presence of magmatic clinozoisite with muscovite, paragonite, quartz, and plagioclase ($\mathrm{An_{15–20}}$) constrains the crystallization of the pegmatites at P–T condition of about 10 kbar and 630 °C ($\mathrm{H_2O}$=1), at the intersection of the reaction curves $\mathrm{Pl_{An15}}$ + Kfs+ W → Czo + Ms + Pg + Qtz and Kfs + Ab + Qtz + W → L (reaction curves 9 and 5, re-

spectively, Fig. 4) (Johannes 1985). Because undeformed pegmatites crosscut the high-grade foliation (Fig. 6), this is a minimum pressure for formation of the high-grade foliation.

Hydration of kyanite, (biotite), and garnet to staurolite + chlorite by the reactions Ky + Bt + W → St + Chl + Ms and Grt + W → St + Chl + Qtz (Thompson 1976) suggests a distinct change in P–T path. Because staurolite does not coexist with biotite, the exhumation trajectory of the Kimi complex passed rapidly through the garnet–staurolite–chlorite stability field during a stage of rapid uplift and cooling (stage C, Fig. 4). Also the replacement of kyanite porphyroblasts by muscovite aggregates and quartz according to the reaction Ky + Kfs + W → Ms + Qtz occurred at this stage.

Ultramafic rocks: structural relationships among successively formed mineral phases

Boudins of metaperidotites scattered throughout the Kimi complex are interpreted as mantle derived.

Spinel–garnet metaperidotites

The overall mineral assemblage of the spinel–garnet metaperidotites is olivine–clinopyroxene–orthopyroxene–spinel (chromian)–garnet–hornblende. Several pre-, syn-, and post-deformation generations of spinel, ortho- and clinopyroxene occur. Macroscopic characteristics are a distinct foliation and lineation defined by flattening (stretching) of large, older clino- and orthopyroxene grains and elongated recrystallized smaller grain aggregates. The grain aggregates were formed by dynamic recrystallization, but were subsequently overprinted during a stage of post-deformational static annealing. Post-deformational mineral assemblages described in the following section document substantial cooling within the stability field of spinel peridotite but at still quite high pressures during ascent. This is indicated by the garnet exsolutions in clinopyroxene from the associated pyroxenites.

Clino- and Orthopyroxenes

Large clino- (Cpx-1) and orthopyroxene-1 (Opx-1) grains contain exsolution lamellae of spinel as well as of ortho- and clinopyroxene, respectively (Figs. 7A, 7B) that formed during cooling. Spinel lamellae are formed at the expense of Ca-Tschermak (Ca-Ts) or Mg-Tschermak (Mg-Ts) components of (Px-1) according to the net transfer reactions Ca-Ts + Ol → Cpx + Spl and Mg-Ts + Ol → Opx + Spl. No garnet exsolution occurred in ortho-and clinopyroxene. Ortho- and clinopyroxene lamellae were later replaced by hornblende.

A second ortho-and clinopyroxene-2 (Px-2) generation is exsolution free and probably formed by dynamic (or static) recrystallization of Px-1. The Al_2O_3 contents of both exsolution-bearing Opx-1 and Cpx-1, and that of exsolution-free Opx-2 and Cpx-2, range from 1.60 to 2.65 wt.% and 0.9 to 2.10 wt.%, respectively. This indicates that Opx-1 and Cpx-1 exsolved their original alumina content during recrystallization and formation of Px-2. Integration of the exsolved alumina in Opx-1 and Cpx-1 yields an original MgAl-Ts + MgCr-Ts component of ~10% in primary Opx-1 and of ~9% CaAl-Ts + CaCr-Ts component in primary Cpx-1, respectively (Table 2).

Garnet

Rare garnet grains (Grs_{13-17} Alm_{22-24} Prp_{58-62} Sps_{1-2} $Uvr_{1.6-2.3}$), commonly with resorbed edges occur only as small inclusions in olivine, spinel (Cr/(Cr + Al) ratio (Cr#) = 0.15) (Spl-2, see later in the text), Opx-2 (Figs. 7C, 7D), and hornblende. Whereas garnet could represent a metastable relict of a primary garnet peridotite, the variation in the Cr content of the garnet and of associated spinel (see the following section) could also suggest that garnet coexisted with Cr-bearing spinel within the garnet–Cr–spinel peridotite stability field.

Spinel

Three successive spinel generations are present:
(1) Large spinel (Spl-1) crystals, interpreted to have formed near maximum P–T conditions, are Cr-rich in their cores with Cr# values ranging from 0.27 to 0.48. Spl-1 crystals include symplectites consisting of spinel (Spl-2, Cr# 0.13), ortho- and clinopyroxene that are interpreted to pseudomorph an older aluminous phase, probably garnet (Fig. 7E). These garnet pseudomorphs show corroded edges, suggesting Spl-1 growth from the inferred older garnet during the first stage of decompression.

(2) During further decompression and cooling, light brown spinel (Spl-2) grew around Spl-1, in the matrix interstitially between exsolution-free smaller Px-2 and as narrowly spaced exsolution lamellae in large Cpx-1 and Opx-1. These Spl-2 grains show Cr# values of 0.12–0.19. There are two generations of spinel lamellae in Opx-1 and Cpx-1 with Cr# 0.17–019 and 0.12–0.14, respectively.

(3) A third generation of spinel (Spl-3) forms symplectites with diopside and enstatite or enstatite and hornblende (Fig. 7F) from the reaction of garnet and olivine grains. The Cr# in the symplectitic Spl-3 ranges from 0.03 to 0.05, which is much lower than the Cr# value (0.13) of the symplectitic Spl-2 included in Spl-1 (Fig. 7E, Table 2) indicating that, during the first stages of decompression and cooling, symplectitic Spl-2 formed at the expense of an older garnet that was richer in Cr content than the garnet associated with formation of Spl-3 symplectites, and that this older garnet coexisted with Spl-1. Ubiquitous and spectacular symplectites of spinel (Spl-3) with enstatite and diopside are also formed at the boundary of alternating layers of garnet pyroxenite and peridotite (millimetre to centimetre thick) by the reaction of garnet from the pyroxenite layer and olivine from the adjacent peridotite layer. In this case, the Cr# of Spl-3 is very low (0.014) because of the low Cr-content of the garnet.

Spinel–garnet clinopyroxenites and clinopyroxene garnetites

Clinopyroxenites occur as layers (millimetre to centimetre scale, locally >1 m wide) within metaperidotite (Figs. 8A, 8B) or as boudins associated with metaperidotites. The layers result from strong flattening and shearing during HP and high-temperature metamorphism. A representative analysis of a spinel–garnet clinopyroxenite has SiO_2, 41.25%; Al_2O_3, 16.88%; FeO_{tot}, 6.79%; MgO, 15.6%; CaO, 16.68%; Na_2O, 0.17%; and TiO_2, 0.21%, giving normative composition with 45.29% anorthite, 0.78% nepheline, 20.4% diopside, 32.86% olivine, and 0.4% ilmenite. Some layers may contain up to 80 vol.% garnet (clinopyroxene garnetites).

Spinel–garnet clinopyroxenites are characterized by the mineral assemblage clinopyroxene + garnet + spinel + hornblende ± olivine, clinopyroxene garnetites by garnet + clinopyroxene + hornblende, and olivine clinopyroxenites by clinopyroxene + olivine ± spinel. A Mg-rich ilmenite (MgO, 5.5%–8.5%) is present in the spinel–garnet clinopyroxenites and clinopyroxene garnetites.

Based on garnet inclusions in olivine (Fig. 8C) and clinopyroxene, clinopyroxenites are interpreted as mantle cumulates that crystallized from melts at high pressure. Subsequently, they are deformed and recrystallized at high temperatures and pressures, above the stability field of

Fig. 7. Spinel–garnet metaperidotite, SEM images. (A) Clinopyroxene (Cpx-1) containing exsolution lamellae of spinel (Spl-2, Cr# = 0.14–0.19) and orthopyroxene (orthopyroxene is replaced by hornblende). (B) Orthopyroxene (Opx-1) containing exsolution lamellae of spinel (Spl-2, Cr# = 0.12–0.19). (C) Garnet inclusion in matrix spinel (Spl-2, Cr# = 0.15). (D) Garnet inclusion in orthopyroxene (Opx-2) that is free of spinel exsolutions. (E) Spl-1 showing compositional zoning (see text). It contains inclusions of spinel (Cr# = 0.13) and orthopyroxene symplectites interpreted as decomposition products of former garnet inclusions, which coexisted with Spl-1. (F) Symplectites of spinel (Spl-3, Cr# = 0.04), with orthopyroxene (Opx-3), clinopyroxene (Cpx-3), and hornblende (Hbl) interpreted as decomposition products of garnet reacted with olivine.
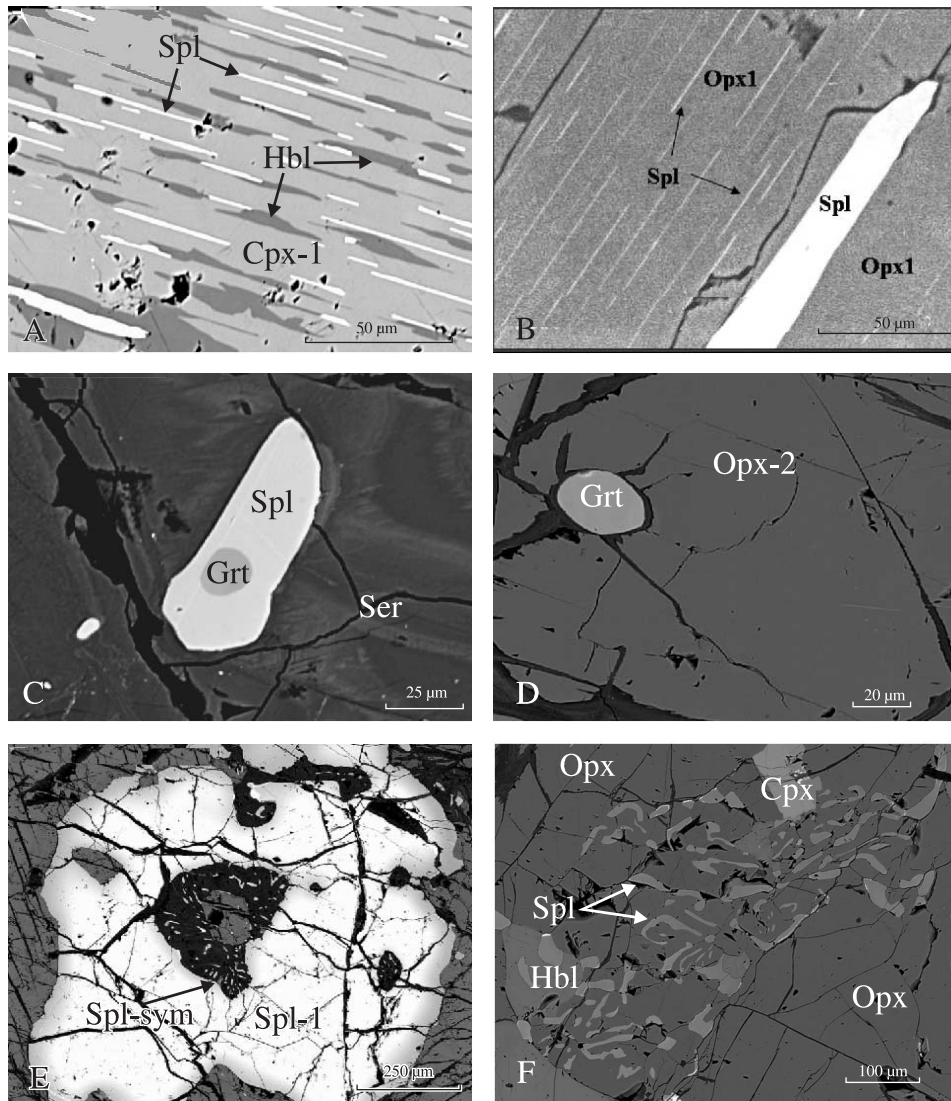
plagioclase. Garnet-clinopyroxenite and garnetite layers may have formed by deformation and metamorphic differentiation between the pyroxenite and adjacent peridotite layer.

Garnet

Garnet forms elongated polycrystalline aggregates characteristically showing homogeneous grain-size distribution, straight grain boundaries, and 120° triple junctions (Fig. 8D). These features reflect static annealing followed by the crystal plastic deformation of garnet. Locally, larger garnet, surrounded by polycrystalline aggregates (Fig. 8E), was observed. The cores of such larger garnet (Grt-1) do not show significant differences in composition compared with the rim and the matrix garnet (Grt-2).

The chemical composition of garnet depends on the bulk-rock composition of the pyroxenites. Garnet composition ranges between $Grs_{21–27}$ $Prp_{45–51}$ $Alm_{24–31}Sps_{0.5–1.2}$ (in olivine-free layers) and $Grs_{16–18}$ $Prp_{51–52}$ $Alm_{28–31}$ $Sps_{1–1.5}$ (in olivine-bearing layers).

Clinopyroxene

Two, pre- and synkinematic clinopyroxene generations can be distinguished. The large pre-kinematic clinopyroxene (Cpx-1, up to 500 µm in length) shows compositional zoning with Al_2O_3 decreasing from ca. 3.5 wt.% (or, if olivine is present from ca. 2.7 wt.%) in the cores to 2.5 wt.% (if olivine is present, to 1.7 wt.%) at the rims. Cpx-1 is interpreted as magmatic clinopyroxene. During cooling, two generations

Table 2. Representative compositions of clinopyroxene, orthopyroxene, garnet, olivine, hornblende, and spinel from the spinel–garnet metaperidotite.

	1 Cpx-2	2 Cpx-1 integ	3 Cpx-3 sym	4 Opx-2	5 Opx-1 integ	6 Opx-3 sym	7 Grt i-Spl	8 Grt i-Opx	9 Grt	10 Ol	11 Hbl	12 Spl-1 core	13 Spl-1 rim	14 Spl-2 matrix	15 Spl-2 ex	16 Spl-2 sym	17 Spl-3 sym
SiO_2	54.72	52.07	54.27	56.78	54.37	56.74	40.93	41.45	41.67	41.18	49.88	—	—	—	—	—	—
TiO_2	—	0.02	—	—	—	—	—	—	—	—	0.26	—	—	—	0.14	—	—
Al_2O_3	0.99	3.50	1.40	1.91	4.30	2.02	22.45	22.82	22.87	—	9.14	35.75	55.31	51.75	50.53	54.30	61.88
Cr_2O_3	0.36	1.10	—	0.24	1.00	—	1.20	0.86	0.95	—	0.82	28.48	11.34	13.47	15.25	12.39	4.84
FeO_t	1.78	2.70	2.05	6.39	6.94	6.85	11.79	11.02	10.10	9.33	3.08	21.78	13.94	15.76	16.41	14.24	12.17
MnO	—	—	—	0.16	0.15	—	1.19	0.66	0.70	—	—	0.28	—	—	—	—	—
MgO	17.83	18.07	17.25	34.78	32.86	33.88	15.84	16.98	17.68	49.28	19.88	13.55	19.23	17.62	17.21	18.45	20.69
CaO	24.63	22.42	24.82	0.21	0.29	0.19	6.20	5.80	5.82	—	12.85	—	—	—	—	—	—
Na_2O	0.08	0.07	—	—	—	—	—	—	—	—	1.06	—	—	—	—	—	—
Total	100.39	99.88	99.79	99.82	99.34	99.68	99.60	99.60	99.80	99.80	97.39	99.84	99.82	99.01	99.54	99.38	99.58
Si	1.976	1.887	1.969	1.960	1.888	1.962	2.993	3.004	2.999	1.006	6.983	—	—	—	—	—	—
Ti	—	0.001	—	—	—	—	—	—	—	—	0.027	—	—	—	0.003	—	—
Al	0.042	0.150	0.073	0.078	0.176	0.082	1.935	1.949	1.972	—	1.508	1.224	1.708	1.647	1.608	1.696	1.858
Cr	0.010	0.032	—	0.006	0.027	—	0.069	0.049	0.054	—	0.091	0.654	0.235	0.288	0.326	0.259	0.097
Fe^{3+}	—	0.045	—	—	—	—	—	—	—	—	—	0.122	0.057	0.065	0.06	0.044	0.045
Fe^{2+}	0.054	0.036	0.062	0.184	0.202	0.198	0.721	0.668	0.614	0.191	0.361	0.407	0.249	0.291	0.310	0.271	0.214
Mn	—	—	—	0.005	0.004	—	0.074	0.040	0.040	—	—	0.007	—	—	—	—	—
Mg	0.959	0.976	0.935	1.756	1.701	1.747	1.727	1.835	1.897	1.796	4.148	0.586	0.751	0.709	0.693	0.729	0.785
Ca	0.953	0.870	0.967	0.008	0.011	0.007	0.486	0.451	0.449	—	1.928	—	—	—	—	—	—
Na	0.006	0.005	—	—	—	—	—	—	—	—	0.228	—	—	—	—	—	—
Total	4.000	4.019	3.997	3.998	4.009	3.996	8.005	7.997	8.025	2.993	15.274	3	3	3	3	2.999	2.999
Cr/(Cr+Al)												0.34	0.12	0.15	0.17	0.13	0.04

Note: Cpx, clinopyroxene; Opx, orthopyroxene; Grt, garnet; Ol, olivine; Hbl, hornblende; Spl, spinel; 2 integ, integrated (1X0.91 + 16X0.05 + 4X0.04); 5 integ, integrated (4X0.95 + 16X0.05); sym, symplectitic replacing garnet + olivine; i-Spl, inclusion in spinel; i-Opx, inclusion in orthopyroxene; ex, exsolution in pyroxene. Fe^{3+}, calculated from FeO_t for four oxygen atoms and three cations. Grt–Cpx thermometry (Ellis and Green 1979). Pair: 1–9 = 715 °C/10 kbar, 730 °C/15 kbar. Al-in-Opx barometry (Brey and Köhler 1990). Pair: 4–8 = 11.9 kbar/700 °C, 16.8 kbar/800 °C. Numbers are cations per oxygenes (6 for Cpx, Opx; 12 for Grt; 4 for Ol, Spl; 23 for Hbl). Major oxides in wt.%.

Fig. 8. Olivine-bearing and olivine-free spinel–garnet pyroxenites. (A, B) Layering of alternating garnet pyroxenite (light) with spinel metaperidotite (dark) subparallel to the high-pressure and high-temperature foliation and lineation. (C) Inclusions of garnet in olivine. SEM image. (D) Polycrystalline garnet aggregates showing straight grain boundaries and 120° triple junctions, reflecting the static annealing stage. (E) Polycrystalline garnet aggregate surround a larger garnet grain. Microphotograph, polarizer only. (F) SEM image of clinopyroxene (Cpx-1) with exsolution lamellae of garnet. (G) Clinopyroxene (Cpx-1) with garnet exsolutions is overgrown by exsolution free clinopyroxene (Cpx-2), which is in equilibrium with garnet (Grt) and olivine (Ol). Microphotograph, half-crossed polars. (H) Spinel–enstatite–diopside symplectites (Sym) replacing garnet and olivine.
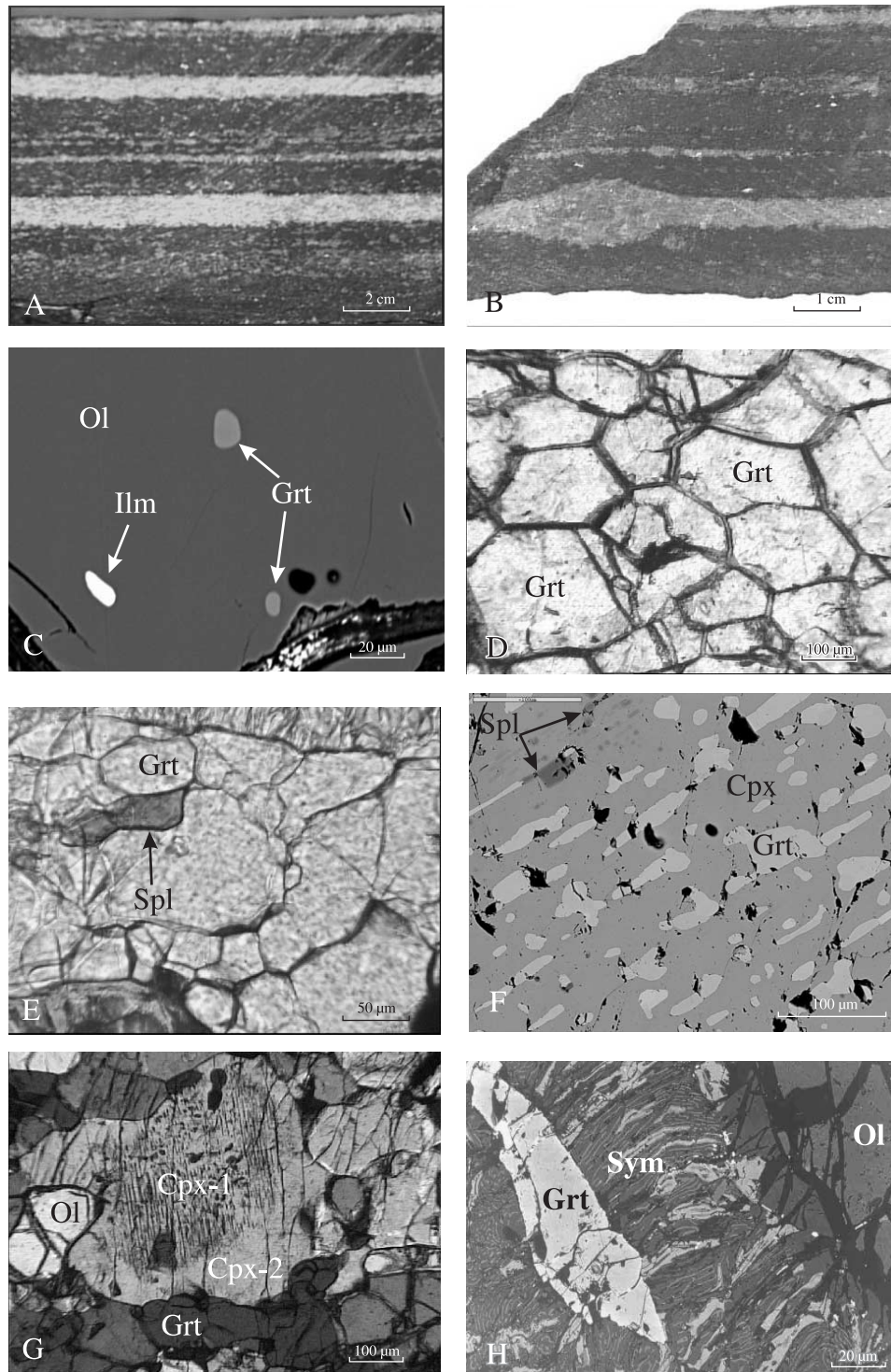
of garnet exsolved in the Cpx-1 cores. Large garnet rods, up to ~300 µm long and 6–10 µm wide, represent the first generation (Figs. 8F, 8G). The second generation consists of very thin garnet rods, ~30–60 µm long and ~2 µm wide, and is associated with exsolved spinel; hence, the original Al_2O_3 content of Cpx-1 was higher (estimated maximum Al_2O_3 content is ~5 wt.%).

A second generation of clinopyroxene (Cpx-2) occurs in polycrystalline ribbons stretched into layers. Such clinopyroxene ribbons are homogeneous in grain size; single grains are internally strain free and show 120° triple junctions. The ribbons are interpreted to have formed by crystal plastic flow and dynamic recrystallization of Cpx-1. The grain-scale fabrics show that intense static annealing and grain growth followed the deformation. Also characteristic is the interstitial growth of spinel and garnet (Grt-2) between Cpx-2 grains in these ribbons.

The exsolution-free rims of Cpx-1 crystals (Fig. 8G) and the exsolution-free Cpx-2 in the ribbons are similar in composition. Also garnet exsolved from Cpx-1, interstitial garnet in the Cpx-2 ribbons, and Grt-2 elongated aggregates are similar in composition. No deformation (bending or kinking) of the exsolved garnet and spinel lamellae was observed, suggesting that formation of the exsolved garnet and spinel in Cpx-1 and of interstitial garnet and spinel within the Cpx-2 ribbons continued through annealing or even postdated the high-temperature deformation.

Spinel

Green spinel occurs as elongated porphyroblasts, up to 1 mm in length, and as smaller interstitial grains between Grt-2 and Cpx-2 grains. Spinel also appears as exsolved lamellas in Cpx-1 or in symplectitic intergrowth (Spl-2) with hornblende, both replacing Cpx–1 and garnet. In olivine-bearing garnet clinopyroxenites, Spl-2 forms symplectites with enstatite and diopside as reaction products from olivine and garnet (Fig. 8F).

Hornblende

Pale-green tschermakitic to pargasitic hornblende (Table 3) forms elongated and oriented grains up to 800 µm in length or smaller grains in textural equilibrium with Cpx-2. In places, hornblende–spinel symplectites replace garnet and clinopyroxene. Inclusions of hornblende in Cpx-2 or spinel, and Cpx-2 or garnet inclusions in hornblende, indicate that these phases crystallized and recrystallized at the same stage of cooling.

Pressure–temperature path of ultramafic rocks

Maximum pressure–temperature conditions

Due to the continuous change of the chemical compositions of the primary minerals during accent and cooling, the record of maximum P–T conditions of the original garnet peridotite is largely erased. However, the metaperidotite clearly documents a metamorphic evolution from the garnet(–spinel) peridotite to spinel peridotite field with a previous mineral assemblage Ol + Opx–1 + Cpx–1 + Grt + Spl–1 (Cr# = 0.27–48) by the presence of garnet inclusions in Spl-2 (Fig. 7C), garnet pseudomorphs within Spl-1 (i.e., symplectitically intergrown

Spl-2 (Cr# = 0.13), Px-2) (Fig. 7E), and the spinel exsolutions in Cpx-1 and Opx-1 (Figs. 7A, 7B). For an assumed temperature of 1000 °C, minimum pressure of 23 kbar is constrained from the association of garnet with Cr–spinel (Cr# = 0.27) (O'Neill 1981). For these P–T conditions, the expected Ca–Ts and Mg–Ts components in Cpx-1 and Opx-1 are ~4% and ~6%, respectively (Gasparik 1984). However, the reintegrated Ca–Ts component in Cpx-1 is ~7.5% and Mg–Ts component in Opx-1 is ~9% (Table 2), implying minimum P–T conditions of ~1200 °C and 25 kbar for the mineral assemblage Ol + Opx-1 + Cpx-1 + Grt + Spl-1 (Cr# = 0.27). Corroded edges of the garnet-pseudomorph inclusions in Spl-1 suggest Spl-1 growth from this previous garnet by the continuous reaction Grt + Ol → Opx + Cpx + Spl-1 (Cr# = 0.27). Therefore, the pressure in the original garnet peridotite was higher than 25 kbar, for an assumed temperature of 1200 °C (O'Neill 1981), and possibly higher than 30 kbar, provided that Spl-1 with the maximum Cr# value (0.48) was formed at the expense of garnet during accent of the original garnet peridotite.

In the associated olivine-bearing spinel–garnet clinopyroxenites, the inclusions of garnet in olivine (Fig. 8C) indicate crystallization of the pyroxenites within the stability field of garnet + olivine. Reintegrating the exsolved garnet (~4% garnet, Table 3) into the core composition of a Cpx-1, the Ca-Ts and the enstatite component of this clinopyroxene yields P–T conditions ~1000 °C and ~18 kbar (Gasparik 1984). These are minimum P–T conditions because olivine-bearing garnet pyroxenites lack orthopyroxene, thus clinopyroxene is not saturated in the enstatite component. It is noteworthy that integration of 1% more garnet into the primary clinopyroxene than that estimated from the exsolutions would only slightly change the estimated P–T conditions. This would increase the Ca-Ts components at 0.35% and decrease the enstatite component at 1.2%, resulting in a lowering of the estimated P–T conditions to ~920 °C and ~16.5 kbar (Gasparik 1984). Garnet–olivine thermometry (O'Neill and Wood 1979) using olivine–garnet inclusion pairs yielded very low temperatures (580–630 °C). These temperatures likely result from retrograde Fe–Mg exchange.

First stage of decompression and cooling

In the spinel–garnet metaperidotite, the Cr# gradually decreases from 0.48 to 0.15 (Table 2) towards the rim of the large Spl-1 crystals. This, together with the continuous decrease of the Cr# in the matrix spinels and formation of clino- and orthopyroxene and spinel exsolution lamellae in Opx-1 and Cpx-1 (Cr# = 0.17–0.19), indicate successive cooling and possible decompression within the enlarged garnet–Cr-bearing spinel peridotite stability field (O'Neill 1981; Brey et al. 1990). Cr# values of <0.19, which are typical for Spl-2 exsolved in Opx-1 and Cpx-1, imply that Spl-1 that coexisted with the garnet had Cr# values >0.19. This suggests lower pressure for the garnet + spinel stability field at 19 to 20 kbar for assumed temperature of 1000 and 1100 °C respectively (O'Neill 1981).

Main equilibration stage: cooling at depth

Textural evidence and inferred mineral reactions, especially in the spinel–garnet pyroxenites, confirm that cooling accompanied by decompression occurred at quite high pressures.

Table 3. Representative compositions of garnet, olivine, clinopyroxene, orthopyroxene, spinel, and hornblende from the spinel–garnet pyroxenites.

	1 Grt i-Ol	2 Grt	3 Grt ex-Cpx	4 Ol	5 Cpx m	6 Cpx-1	7 Cpx-1 integ	8 Cpx-3 sym	9 Opx sym	10 Spl-2 sym	11 Grt ex-Cpx	12 Grt m	13 Cpx-1 core	14 Cpx-2 rim	15 Hbl	16 Spl m	17 Spl ex-Cpx
SiO_2	40.70	41.00	40.70	40.00	53.85	53.15	53.12	54.15	56.48	—	41.20	41.20	52.36	52.46	45.54	—	—
TiO_2	—	—	—	—	0.28	0.27	0.22	—	—	—	—	—	0.30	0.27	0.46	—	—
Al_2O_3	22.90	23.00	23.00	—	1.93	2.28	3.18	1.16	2.07	63.27	23.30	23.30	3.21	3.13	13.46	63.99	64.60
Cr_2O_3	0.23	0.26	0.16	—	—	—	0.03	—	—	1.11	—	—	—	—	—	0.19	—
FeO_t	15.70	14.94	13.81	14.30	2.68	2.80	3.12	2.80	9.80	15.93	13.58	13.60	2.73	2.72	4.97	15.27	14.19
MnO	0.79	0.50	0.46	—	—	—	0.02	—	—	—	0.46	0.40	—	—	—	—	—
MgO	14.06	14.22	14.29	45.30	16.86	16.76	17.20	16.89	31.97	18.97	14.10	13.90	17.00	17.30	18.21	20.46	21.26
CaO	6.11	6.20	6.93	—	24.45	24.61	23.74	24.80	0.21	—	8.00	8.03	24.37	23.93	12.43	—	—
Na_2O	—	—	—	—	—	—	—	—	—	—	—	—	0.07	0.09	1.55	—	—
Total	100.09	100.12	99.35	99.60	100.04	99.47	100.63	99.80	100.53	99.43	100.64	100.43	100.04	99.90	96.62	99.91	100.05
Si	2.992	3.005	2.998	1.003	1.957	1.939	1.920	1.976	1.962	—	2.998	3.003	1.908	1.912	6.478	—	—
Ti	—	—	—	—	0.008	0.007	0.006	—	—	—	—	—	0.008	0.007	0.049	—	—
Al	1.990	1.987	1.997	—	0.083	0.098	0.135	0.050	0.085	1.911	1.998	2.001	0.138	0.134	2.566	1.904	1.908
Cr	0.013	0.015	0.009	—	—	—	—	—	—	0.022	—	—	—	—	—	0.004	—
Fe^{3+}	—	—	—	—	—	—	—	—	—	0.066	—	—	—	—	—	0.092	0.092
Fe^{2+}	0.934	0.916	0.851	0.300	0.081	0.085	0.094	0.085	0.285	0.275	0.826	0.829	0.083	0.083	0.591	0.230	0.206
Mn	0.049	0.031	0.029	—	—	—	—	—	—	—	0.028	0.025	—	—	—	—	—
Mg	1.541	1.554	1.569	1.694	0.913	0.912	0.927	0.918	1.656	0.725	1.529	1.510	0.923	0.938	3.861	0.770	0.794
Ca	0.481	0.487	0.547	—	0.952	0.962	0.920	0.970	0.008	—	0.624	0.627	0.951	0.934	1.894	—	—
Na	—	—	—	—	—	—	—	—	—	—	—	—	0.005	0.006	0.427	—	—
Total	8.00	7.995	8.000	2.997	3.994	4.003	4.002	3.999	3.996	2.999	8.003	7.995	4.016	4.014	15.866	3	3

Note: Analyses 1 to 10 are from olivine-bearing garnet clinopyroxenite and 11 to 17 from spinel–garnet clinopyroxenite. Analysis 14 is exsolution-free rim of Cpx-1. Grt, garnet; Ol, olivine; Cpx, clinopyroxene; Opx, otthopyroxene; Spl, spinel; Hbl, hornblende; i-Ol, inclusion in olivine; ex-Cpx, exsolution in clinopyroxene; m, matrix; integ, intergrated (6X0.96 + 3X0.04); sym, symplectites replacing garnet + olivine. Grt–Cpx thermometry (Ellis and Green 1979). Pairs: 3–6 = 749 °C; 11–13 = 765 °C; 12–14 = 757 °C for 15 kbar. Grt–Ol thermometry (O'Neill and Wood 1979). Pairs: 1–4 = 588 °C, 2–4 = 607 °C. Numbers are cations per oxygenes (12 for Grt; 4 for Ol, Spl; 6 for Cpx, Opx; 6 for Hbl). Major oxides in wt.%.

Fig. 9. *P–T–t* diagram showing the exhumation path of the metaperidotites and pyroxenites of the mantle assemblage in the ultra-high-pressure metamorphic Kimi complex (eastern Rhodope Mountains). A–C are different stages discussed in the text. 1–5 are the reaction curves.
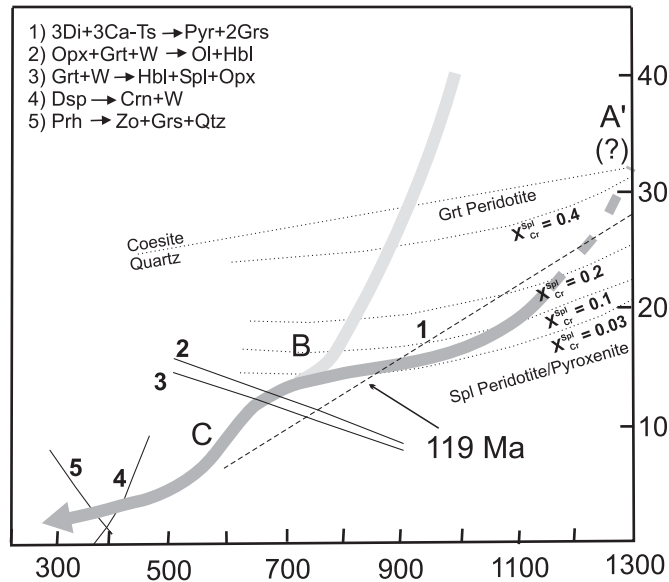
The exsolution of garnet from Cpx-1 in spinel–garnet pyroxenites and garnet pyroxenites indicates that cooling occurred within the garnet-pyroxenite stability field. Garnet-clinopyroxene geothermometry (Ellis and Green 1979), using exsolving garnet–clinopyroxene host and matrix garnet – exsolution free clinopyroxene pairs, yielded equilibration temperatures of 750–765 °C for assumed pressure of 15 kbar (Table 3). The reaction 3 Di + 3 Ca-Ts → Pyr + 2 Grs calculated for exsolved garnet–clinopyroxene host, with the Thermo-Calc program of Holland and Powell (1998), constrains minimum pressures of ~11 kbar at 750 °C for this stage of cooling (reaction curve 1, Fig. 9).

The Cr-bearing spinel exsolutions in Opx-1 and Cpx-1 from peridotite and the interstitial Spl-2 (Cr# = 0.10–0.19), which are associated with exsolution-free Opx-2, Cpx-2, and olivine, indicate cooling of the peridotite within the spinel-peridotite stability field. Garnet in peridotite is only found as rare inclusions in Spl-2, (Cr# = 0.15), Opx-2 (Figs. 7C, 7D), Ol and later formed Hbl. Assuming that garnet was in equilibrium with the host Opx-2, pressures of 10.6–11.9 kbar for 700 °C and 15.5–16.8 kbar for 800 °C are obtained with the Al-in orthopyroxene barometer of Brey and Köhler (1990) (Table 2).

In pyroxenites, Grt-2 (exsolution and matrix), Cpx-2 (matrix grains and rim of Cpx-1), spinel, hornblende, and, if present, olivine are in textural equilibrium with each other. Similarly, Opx-2, Cpx-2, Spl-2, and Hbl are in textural equilibrium in the metaperidotite. This is a clear indication that these *P–T* conditions prevailed during static annealing, and thus that the deformation must have occurred at higher pressures and temperatures.

Symplectites of enstatite–diopside–spinel (Cr# = 0.03–0.05) in the metaperidotite and diopside–enstatite–spinel (Cr# = 0.012) between adjacent garnet grains of the garnet pyroxenite and olivine grains of the peridotite layer record

the transition of the garnet peridotite and pyroxenite stability field to that of spinel peridotite and pyroxenite, according to the reaction Grt + Ol (Fo 0.9) → Opx + Cpx + Spl (Cr# = <0.05), constraining this reaction at *P* < 14 kbar for an assumed temperature of 700 °C (O'Neill 1981; Gasparik 1984).

It is important to note that, after ascend to a depth corresponding to about 15 kbar, at ~15 to 12 kbar, the mantle assemblage experienced substantial cooling from ~1100 °C to <700 °C (cooling path B, Fig. 9).

The formation of chromian hornblende (Si = 6.5–6.9 atoms per formula unit; Cr_2O_3, 0.8–1.1 wt.%; Al_2O_3, 8–11 wt.%) coexisting with olivine indicates hydration reactions like Grt + Opx + W → Ol + Hbl and Opx + Cpx + Spl + W→ Hbl + Ol taking place below 13–12 kbar at 650–750 °C (reaction curve 2, Fig. 9). At similar *P–T* conditions, Hbl + Spl (Cr# = 0.04) + Opx symplectites replaced pseudomorphically garnet (reaction curve 3, Fig. 9).

Discussion

In summary, the *P–T* data and textural observations, together with their correlation with already published geochronological data of both the mantle and continental crustal rocks, suggest that: (1) mantle and crustal rocks may have been exhumed from different initial depths and thus may have unrelated early histories; (2) mantle and crustal rocks have a common ascend history only from a depth corresponding to ~15 kbar upward; and (3) both crustal and mantle rocks may have undergone complex and polyphase ascend histories.

Some recent U–Pb zircon, Sm–Nd garnet–clinopyroxene–whole- rock, and Rb–Sr mica data from various rock types of the Rhodope domain give ages ranging between ~150 and 63 Ma, which are consistent with a polyphase metamorphic evolution of the Kimi complex. However, a correlation of the geochronological data with the *P–T* paths and tectono-metamorphic processes inferred from the microtextures is still ambiguous. Nevertheless, the present data are consistent with the idea that crustal and mantle rocks underwent different early metamorphic histories.

Ultra-high-pressure metamorphism and exhumation path of metapelites

The correlation of the *P–T* path with deformation fabrics of the metapelites, and geochronological data put forward a polyphase ascent and exhumation history.

Peak *P–T* conditions of ~>45 kbar at ~1000 °C imply very low viscosity of the diamondiferous metapelites. At such metamorphic conditions, dehydration melting is expected, e.g., through the breakdown of phengite (Hermann and Green 2001). A number of petrological and textural observations support partial melting of the diamond-bearing migmatitic metapelites, such as leucocratic and melanocratic layers resulting form melt segregation, and an isoclinally folded and transposed stromatic layering, indicating that melt crystallization associated with deformation. Partial melting probably occurred at the maximum depth and the early ascend stages, from pressures of >45 kbar (corresponding to a depths of ~150 km) to pressures of ~20–16 kbar (corresponding to

depths of ~65–55 km), which was probably combined with some cooling.

For the Kokchetav massif in Kazakhstan, Hermann et al. (2001) and Massonne (2003) concluded that the subducted slab underwent partial melting of the metapelites. Partial melting might have a significant effect on the rheology of the subducted rocks. Melts might have enhanced detachment of the diamond-bearing gneisses from the slab and lubricated contacts during fast ascent. Buoyancy forces of the partially molten crustal rocks could provide the driving force for uplift. Cooling combined with ascent of the metapelites from a depth of ~150 km to a depth corresponding to 16 kbar (~55 km) indicates their ascend along a subduction channel.

Increased cooling relative to decompression occurred at ~16–12 kbar from at least 800 °C to ~650 °C. At this stage, pervasive re-equilibration of the UHP assemblages occurred. Most mineral reactions are hydrous. Characteristically, microfabrics of minerals indicate static grain growth and annealing.

At pressures lower than ~12 kbar, decompression under amphibolite-facies conditions occurred, followed by cooling at shallow depths, below 5 kbar. Further hydration during these stages is respectively documented by widespread formation and intrusion of muscovite pegmatites in the crustal and mantle derived rocks and the replacement of olivine, hornblende, garnet, spinel, and clinopyroxene by antigorite, tremolite, chlorite, diaspore, and prehnite along hydration channels at pressures <4 kbar in the mantle rocks (Mposkos et al. 1994). Shear zones formed from amphibolite-facies through greenschist-facies conditions. They dismembered the large ultramafic bodies into boudins ranging in size from 1 m to 500 m in scale and are probably related with the final emplacement of the Kimi complex at upper crustal levels.

This stage of increased decompression under amphibolite-facies conditions and successive cooling at a shallow crustal depth probably reflects acceleration of crustal thickening owing to a continental collision episode (Stage D, Fig 10; see later in the text). In this stage, nappe-stacking pushed the Kimi complex toward a higher structural position. This thickening probably initiated the formation of low-angle detachment that ultimately exhumed the Kimi complex (orogenic "collapse"). In the present state, a low-grade metamorphic unit overlies the Kimi complex in the eastern Rhodope Mountains (eastern Circum Rhodope Zone), suggesting that a low-angle extensional detachment must have been responsible for denudation of the Kimi complex rather than erosion (Krohe and Mposkos 2002).

Metamorphic zircon rims from paragneisses of the Central Rhodope Mountains, for which UHP-metamorphism has been suggested, yielded a $^{206}Pb/^{238}U$ sensitive high-resolution ion microprobe (SHRIMP) (lower intercept) age of 148.8 ± 2.2 Ma that is interpreted as approximating the UHP stage in these rocks (Liati 2005). Importantly, this age is significantly older than (1) the range of $^{206}Pb/^{238}U$ SHRIMP ages from metamorphic zircons from the eclogites (metabasites) and (2) the Sm–Nd garnet–clinopyroxene–whole-rock age from the pyroxenes of the mantle assemblage (see later in the text).

Geochronological data from pegmatoids that intrude both mantle and crustal rocks comprise $^{206}Pb/^{238}U$ zircon ages and Rb–Sr ages of magmatically formed muscovite yielding 61 ± 1.9 and 65 ± Ma, respectively (Liati et al. 2002; and Mposkos and Wawrzenitz 1995). They provide a reliable time constraint for the intrusion of pegmatoids and of the late exhumation stages of both crustal and mantle rocks. This long-lasting tectonometamorphic history suggests that ascent of the UHP rocks from maximum depths and their final emplacement in the upper crust occurred by dissimilar, temporally separated tectonic mechanisms.

Trondhjemitic dykes crystallized at a pressure of about 10 kbar (Mposkos 2002), corroborating that pervasive deformation occurred at pressures higher than 10 kbar. Indicators for UHP metamorphism are not observed in these rocks.

Pressure–temperature path of metaperidotites

Mantle rocks experienced pressures higher than 30 kbar because the protolith of the spinel–garnet metaperidotite was garnet peridotite that equilibrated at $P > 30$ kbar (Fig. 9). This is corroborated by the Spl-2 (Cr# = 0.13)–Px symplectite inclusions replacing earlier garnet inclusions in Spl-1 (maximum Cr# = 0.48). However, equilibration at later stages and at still high temperatures destroyed most of the original mineral assemblages thus hampering estimation of the peak $P–T$ conditions.

Partial melting of the metaperidotites is shown by the occurrence of spinel–garnet-pyroxenite and garnet-pyroxenite layers within the metaperidotites, interpreted as cumulates. Crystallization of the melt and formation of cumulate pyroxenites occurred at high pressures, within the stability field of garnet pyroxenite, as indicated by the garnet inclusions in olivine and in Cpx-1 from the garnet pyroxenite. However, the present geochronological data do not constrain the formation ages of the garnet pyroxenites. It is therefore unclear if melting occurred with the influx of water released from descending slab or if it is related to an older event that could be unrelated to the Alpine subduction and exhumation history.

Although subsequent annealing (Figs. 8D, 8E) erased most of the original mineral assemblage, relict fabrics in spinel–garnet pyroxenites clearly imply high-temperature deformation (Fig. 8B) including the plastic flow of garnet.

Annealing of the mantle rocks correlates with substantial cooling and only with little exhumation. The ultramafic assemblages allow more accurate temperature estimates for this stage, and they suggest cooling from temperatures higher than 1000 °C. Near isobaric cooling occurred within the garnet-pyroxenite stability field as indicated by the garnet-exsolution lamellae in Cpx-1 of the pyroxenites (stage B, Fig. 9). This stage occurred at depth corresponding to lower crustal depth of a thickened continental crust, indicating a significant decrease in the exhumation rate and probably accretion of the ultramafic assemblage of the future Kimi complex at the base of the overriding continental plate.

Generally no deformation occurred under these conditions. All microfabrics indicate static annealing at this stage. Some of the mineral reactions that occurred during static annealing are hydration reactions, indicating the presence of water during this stage. The absence of deformation implies that the overriding continental plate including the Kimi complex was decoupled from the subducting plate at that stage. Thus minor exhumation at this stage was probably accom-

Fig. 10. Tentative tectonic evolution of the Kimi complex including subduction of continental material to mantle depths (Stage A), possible slab break-off and upwelling of hot mantle (Stage B), amalgamation of the ultra-high-pressure continental material and mantle rocks at the base of the (thickened) overriding continental plate (Stage C), and final exhumation of the Kimi complex from the lower crust associated with a second collision episode (Stage D) (see text for further explanation).
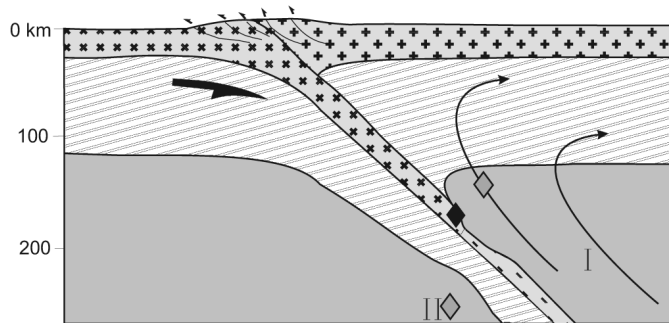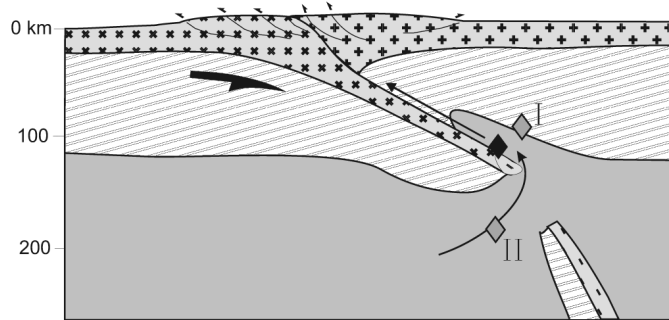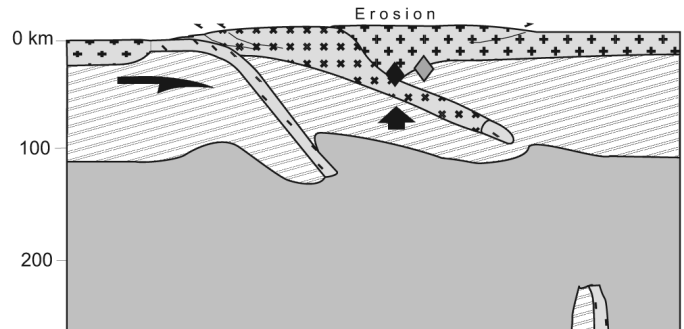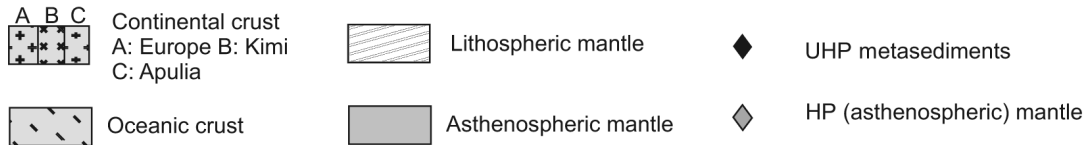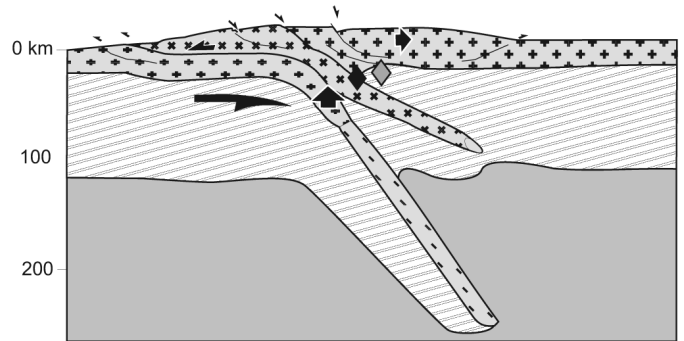
modated by erosion and not by some tectonic process. Some of the undeformed trondhjemitic dykes (Fig. 6) intruded at about 10 kbar and crosscut the foliation and (or) lineations were possibly formed at this stage.

From a correlation of the geochronological data with petrology and microtextural data, the following constraints can be derived. A Sm–Nd garnet–clinopyroxene–whole-rock age from a spinel–garnet pyroxenite described herein yielded an age of 119 ± 3.5 Ma (Wawrzenitz and Mposkos 1997). If this age reflects equilibrium conditions, it most likely reflects Grt-2 and Cpx-2 growth and thus a post-peak pressure, HP-metamorphic stage. Grt-2 is quite homogeneous, and Grt-1 is only a small fraction of the overall garnet volume, ruling out that this age resulted from a mixture between pre-kinematic Grt-1 and syn- and post-kinematic Grt-2. The analyzed clinopyroxene fraction entirely consisted of spinel-free recrystallized grains.

Correlating Grt-2 growth with the microtextural evolution implies that this may also be an age constraint for (1) the static annealing stage in the mantle assemblage, and (2) a minimum age for pervasive plastic deformation and the earlier attained maximum pressures. Because plastic deformation of

mantle rocks occurred at temperatures above 765 °C in accord with microfabrics suggestive of plastic flow of garnet (e.g. Voegelé et al. 1999; Storey and Prior 2005) and annealing below 15 kbar, we consider the Sm–Nd garnet–clinopyroxene–whole-rock age of this spinel–garnet pyroxenite of 119 Ma as unrelated to UHP metamorphism that was recorded in metapelites.

Liati et al. (2002) obtained U–Pb SHRIMP ages from zircons from the "eclogitic" (garnet-rich mafic) rock, which may suggest that the metamorphic history of metabasites correlates with that of the metaperidotites rather than with that of the metasedimentary rocks. Oscillatory zoned grains, typical for zircons, crystallized from melts or fluids yielded $^{206}Pb/^{238}U$ ages of 117.4 ± 1.9 Ma (Liati et al. 2002). The occurrence of quartz inclusions in the zircons dated by Liati et al. (2002) corroborate that zircons did not crystallize under UHP conditions but possibly under eclogite and granulite-facies conditions. Liati et al. (2002) interpreted this age either as a magmatic protolith formed at a mid-ocean ridge or as a garnet-clinopyroxene cumulate formed from mantle melts at UHP conditions, implying that the eclogites record a separate stage of UHP metamorphism that is signif-

icantly younger than that of the metasediments. It should be noted that the occurrence of quartz inclusions in such zircons preclude their formation during the UHP stage. Textural evidence indicate intense post-eclogitic recrystallization and possible partial melting. The "garnet-rich mafic" rock contains scapolite + hornblende-rich pockets replacing garnet and clinopyroxene, and some mm to several cm thick trondhjemitic veinlets (Baziotis et al. 2006). It is possible that the age of 117 Ma represents zircon crystallization from a sulphate rich fluid or from a melt at this stage (static-annealing stage).

Separate early metamorphic histories of ultra-high-pressure metapelites and metaperidotites

The record of different P–T–t (time) paths between UHP metapelites and HP mantle rocks suggests that both originate from different parts of the lithosphere and have been brought together during a tectonic event postdating UHP metamorphism. P/T ratio during peak P–T conditions of the UHP metapelites and cooling during their ascent are typical for metamorphism and exhumation of HP rocks within a subduction channel. However, the high Al_2O_3 content (~5 wt.%) of the cumulus Cpx-1 in the pyroxenite and of Opx-1 (~4.3 wt.%) and Cpx-1 (~3.5 wt.%) in the metaperidotite (Tables 2, 3) clearly indicates that partial melting of peridotite, and the crystallization of melt including the cumulus pyroxenites (>1000 °C, 18 kbar) must have occurred somewhere outside of the subduction channel.

Moreover, the present geochronological data seem to suggest that the respective maximum P–T conditions in UHP metapelites and metaperidotites could have occurred at different times. In this case, hot peridotites originated from underneath the overriding continental plate, and their ascent to depths corresponding to about 45 km (i.e., the base of a thickened crust) is unrelated to the ascent of UHP metapelites. This is in agreement with the shapes of the two P–T paths that suggest separate ascend histories at pressures higher than 15 kbar for metapelites and metaperidotites.

A possible mechanism of ascend of deep-seated rocks in the mantle wedge is mantle convection possibly in association with formation of a magmatic arc or back-arc extension (Stage A, path I, Fig. 10). High-temperature deformation in the mantle rocks may reflect mantle convection.

Alternatively the protolith of the metaperidotites may represent an asthenospheric mantle segment incorporated into the subduction channel. In this case, juxtaposition of mantle against continental crustal material from the subducted plate and ascend of both would be related mechanisms. A possible mechanism would be upwelling of hot asthenospheric mantle into the mantle wedge following possible slab break-off from the subducted oceanic lithosphere (after collision) (Stages A, B, path II, Fig. 10). Models involving slab break-off have been described as mechanisms of exhumation of deeply subducted crustal terranes (see references in Brückner and Medaris 2000). Such a mechanism could account for the observed high temperatures, the high-temperature deformation, and the subsequent dramatic cooling of the mantle rocks. The high-temperature deformation of the mantle assemblage could reflect mantle convection related to upwelling of asthenospheric mantle associated with slab break-off, above the subduction zone (Stage B, path II, Fig. 10). However, in this case, crustal and mantle rocks are expected to have juxtaposed against each other within the mantle, and not, as the P–T paths suggest, at the base of a thickened continental crust.

Joint late-metamorphic histories of UHP metapelites and metaperidotites

Subsequently, from ~16–14 kbar onward, mantle and former UHP metapelites ascended together (Stage C, Fig. 10). Continuing decompression and cooling occurred first within the enlarged stability field of garnet–Cr–spinel peridotite (O'Neill 1981), as suggested by the garnet inclusions in Spl-2 (Cr# = >0.15), and then into the Cr-spinel peridotite field, as indicated by the spinel exsolution in Opx-1 and Cpx-1. At this stage, the mantle material and the former UHP metapelites juxtaposed at the base of the lower crust of the continental margin from the overriding plate (Stage C, Fig. 10).

Geotectonic setting

If the age of UHP metamorphism of about 150 Ma is corroborated by future investigations, the Kimi complex documents the presence of an active continental margin during the Jurassic in the eastern Rhodope Mountains associated with the subduction of the northern branch of the Tethys underneath the European plate along the Vardar zone (Ricou et al. 1998). The ultrabasic rocks may have been incorporated into the Kimi complex during their ascent, in the course of a continuing subduction process.

Successively, near-isobaric cooling and associated hydration of all the Kimi complex occurred until 62–65 Ma, which was the formation age of the pegmatites still showing an intrusion depth corresponding to about 25–30 km. This long-continuing cooling history during ascent suggests a continuing subduction of cool material including water-rich sediments underneath the European plate, which includes the entire the Kimi complex (Stages C, D, Fig. 10). These stages may be associated with subduction of an extended continental margin and (or) marginal basins temporally related to an oceanic basin corresponding to southern branch of the Tethys ("Pindos ocean") (Stampfli and Pillevuit 1993; Robertson et al. 1996).

Possibly this stage correlates with the subduction of the structurally lower parts of the Rhodope domain (segment 2, Krohe and Mposkos 2002) that show a substantially younger HP metamorphism underneath the Kimi complex. Soon after this stage, accelerated crustal thickening below the Kimi complex (Stage D, Fig. 10) led to its ultimate exhumation: in this stage, thrusting of the Kimi complex upon the younger HP units of segment 2 occurs and possibly the normal faults at the top of the Kimi complex are formed. Before 48 Ma (Lutetian), immediately after its denudation, sedimentary basins formed on the Kimi complex.

Acknowledgments

helped to improve style and content of the article substantially.

References

Akaishi, M., Shaji Kumar, M.D., Kanda, H., and Yamaoka, S. 2000. Formation process of diamond from supercritical H_2O-CO_2 fluid under high pressure and high temperature conditions. Diamond and Related Materials, **9**: 1945–1950.

Anovitz, L.M., and Essene, E.J. 1987. Phase equilibria in the system $CaCO_3$–$MgCO_3$–$FeCO_3$. Journal of Petrology, **28**: 389–414.

Baziotis, I., Mposkos, E., and Perdikatsis, V. Geochemistry of amphibolitized eclogites and cross-cutting trondhjemitic dykes in the ultra-high pressure metamorphic Kimi Complex in East Rhodope. International Journal of Earth Sciences. Under review.

Brey, G.P., and Köhler, T. 1990. Geothermobarometry in four-phase lherzolites II. New thermobarometers, and practical assessment of existing thermobarometers. Journal of Petrology, **31**: 1353–1378.

Brey, G.P., Köhler, T., and Nickel, K.G. 1990. Geothermobarometry in four-phase lherzolites I. Experimental results from 10 to 60 kbar. Journal of Petrology, **31**: 1313–1352.

Brückner, H.K., and Medaris, L.G. 2000. A general model for the intrusion and evolution of mantle garnet peridotites in high-pressure and ultra-high pressure metamorphic terranes. Journal of Metamorphic Geology, **18**: 123–133.

Burg, J.P., Ricou, E., Ivanov, Z., Godfriaux, I., Dimov, D., and Klain, L. 1996. Syn-metamorphic nappe complex in the Rhodope Massif: structure and kinematics. Terra Nova, **8**: 6–15.

Dinter, D.S. 1998. Late Cenozoic extension of the Alpine collisional orogen, northeastern Greece: origin of the north Aegean basin. Geological Society of America Bulletin, **110**: 1208–1230.

Dinter, D.A., Macfarlane, A., Hames, W., Isachsen, C., Bowering, S., and Royden, L. 1995. U–Pb and $^{40}Ar/^{39}Ar$ geochronology of the Symvolon granodiorite: implication for the thermal and structural evolution of the Rhodope metamorphic core complex, northern Greece. Tectonics, **14**: 886–908.

Dobrzhinetskaya, L.F., Green, H.W., Bozhilov, K.N., Mitchell, T.E., and Dickerson, R.M. 2003. Crystallization environment of Kazakhstan microdiamond: evidence from nanometric inclusions and mineral associations. Journal of Metamorphic Geology, **21**: 425–437.

Ellis, D.J., and Green, D.H. 1979. An experimental study of the effect of Ca upon garnet-clinopyroxene Fe–Mg-exchange equilibria. Contributions to Mineralogy and Petrology, **71**: 13–22.

Ferry, J.M., and Spear, F.S. 1978. Experimental calibration of the partitioning of Fe and Mg between biotite and garnet. Contributions to Mineralogy and Petrology, **66**: 113–117.

Gasparik, T. 1984. Two-pyroxene thermobarometry with new experimental data in the system CaO–MgO–Al_2O_3–SiO_2. Contributions to Mineralogy and Petrology, **87**: 87–97.

Harland, W.B., Armstrong, R.L., Cox, A.V., Craig, L.E., Smith, A.G., and Smith, D.G. 1990. A geologic time scale 1989. Cambridge University Press, Cambridge, UK, 263 p.

Hermann, J., and Green, D.H. 2001. Experimental constraints on high pressure melting in subducted crust. Earth and Planetary Science Letters, **188**: 149–186.

Hermann, J., Müncener, O., Trommsdorff, V., Hansmann, W., and Piccado, G.B. 1997. Fossil crust to mantle transition, Val Malenco (Italian Alps). Journal of Geophysical Research B, **102**(9): 20 123 – 20 132.

Hermann, J., Rubatto, D., Korsakov, A., and Shatsky, V.S. 2001. Multiple zircon growth during fast exhumation of diamondiferous, deeply subducted continental crust (Kokchetav Massif, Kazakhstan). Contributions to Mineralogy and Petrology, **141**: 66–82.

Holland, T.J.B., and Powell, R. 1998. An internally-consistent thermodynamic dataset for phases of petrological interest. Journal of Metamorphic Geology, **16**: 309–344.

Johannes, W. 1985. The significance of experimental studies for the formation of migmatites. *In* Migmatites. *Edited by* Ashworth. Blackie, New York, N.Y., pp. 36–85.

Kennedy, C.S., and Kennedy, G.G. 1976. The equilibrium boundary between graphite and diamond. Journal of Geophysical Research, **81**: 2467–2470.

Koziol, A.M., and Newton, R.C. 1988. Redetermination of the anorthite breakdown reaction and improvement of the Plagioclase–Garnet–AL2SIO5–Quartz geobarometer. American Mineralogist, **73**(3–4): 216–223.

Kretz, R. 1983. Symbols for rock-forming minerals. American Mineralogist, **68**: 277–279.

Krohe, A., and Mposkos, E. 2002. Multiple generations of extensional detachments in the Rhodope mountains (northern Greece): evidence of episodic exhumation of high-pressure rocks. *In* The timing of location of major ore deposits in an evolving orogen. *Edited by* D.J. Blundell, F. Neubauer, and, A. Quadt. Geological Society (of London), Special Publications 204, pp. 151–178.

Le Breton, N., and Thompson, A. 1988. Fluid-absent (dehydration) melting of biotite in metapelites in the early stages of crustal anatexis. Contributions to Mineralogy and Petrology, **99**: 226–237.

Liati, A. 2005. Identification of repeated alpine (ultra) high-pressure metamorphic events by U–Pb SHRIMP geochronology and REE geochemistry of zircon: the Rhodope zone of Northern Greece. Contributions to Mineralogy and Petrology, **150**: 608–630.

Liati, A., and Seidel, E. 1996. Metamorphic evolution and geochemistry of kyanite eclogites in central Rhodope, northern Greece. Contributions to Mineralogy and Petrology, **123**: 293–307.

Liati, A., and Gebauer, D. 1999. Constraining the prograde and retrograde *P–T–t* path of Eocene HP rocks by SHRIMP dating of different zircon domains: inferred rates of heating, burial, cooling and exhumation for central Rhodope, northern Greece. Contributions to Mineralogy and Petrology, **135**: 340–354.

Liati, A., Gebauer, D., and Wysoczanski, R. 2002. U–Pb SHRIMP-dating of zircon domains from UHP garnet-rich mafic rocks and late pegmatoids in the Rhodope zone (N. Greece); evidence for Early Cretaceous crystallization and Late Cretaceous metamorphism. Chemical Geology, **184**: 281–299.

Lips, A.L.W., White, S.H., and Wijbrans, J.R. 2000. Middle-Late Alpine thermotectonic evolution of the southern Rhodope Massif, Greece. Geodinamica Acta, **13**(5): 281–292.

Massonne, H.J. 1999. A new occurrence of microdiamonds in quartzofeldspathic rocks of the Saxonian Erzgebirge, Germany and their metamorphic evolution. *In* Proceedings VIIth International Kimberlite Conference, Cape Town, South Africa, 1998. *Edited by* J.J. Gurney, J.L. Gurney, M.D. Pascoe, and S.H. Richardson. Red Roof Publ., South Africa, The P.H. Nixon Vol. 2, pp. 533–539.

Massonne, H.-J. 2001. Origin of microdiamond bearing quartzofeldspathic rocks (saidenbachites) from Erzgebirge, Germany: a progress report. *In* UHPM Workshop 2001. Fluid–slab–mantle interaction and ultrahigh-P minerals, Waseda University, Tokyo, Japan, Abstract Vol. Paper 1A03, pp. 11–15.

Massonne, H.-J. 2003. A comparison of the evolution of diamondiferous quartz rich rocks from Saxonia, Erzgebirge and the

Kokchetav Massif: are so-called diamondiferous gneisses magmatic rocks? Earth and Planetary Science Letters, **216**: 347–364.

Massonne, H.-J., and O'Brien, P.I. 2003. The Bohemian Massif and the NW Himalaya. European Mineralogical Union. Notes in Mineralogy, **5**(6): 145–187.

Massonne, H.-J., and Szpurka, Z. 1997. Thermodynamic properties of white micas on the basis of high-pressure experiments in the systems $K_2O–MgO–Al_2O_3–SiO_2–H_2O$ and $K_2O–FeO–Al_2O_3–SiO_2–H_2O$. Lithos, **43**: 229–250.

Mposkos, E. 1989. High-pressure metamorphism in gneisses and pelitic schists in the East Rhodope Zone (N. Greece). Mineralogy and Petrology, **41**: 25–39.

Mposkos, E. 2002. Petrology of the ultra-high pressure metamorphic Kimi complex in Rhodope (N.E. Greece): A new insight into the Alpine geodynamic evolution of the Rhodope. Bulletin of Geological Society Greece, **XXXIV**(6): 2169–2188.

Mposkos, E., and Kostopoulos, D. 2001. Diamond, former coesite and supersilicic garnet in metasedimentary rocks from the Greek Rhodope: a new ultrahigh-pressure metamorphic province established. Earth and Planetary Science Letters **192**: 497–506.

Mposkos, E., and Krohe, A. 2000. Petrological and structural evolution of continental high pressure (HP) metamorphic rocks in the Alpine Rhodope Domain (N. Greece). *In* Proceedings of the 3rd International Conference on the Geology of the Eastern Mediterranean, Nicosia, Cyprus, 1999. *Edited by* I. Panayides, C. Xenophontos, and J. Malpas. Geological Survey, Nicosia, Cyprus, pp. 221–232.

Mposkos, E., and Liati, A. 1993. Metamorphic evolution of metapelites in the high-pressure terrane of the Rhodope zone, Northern Greece. Canadian Mineralogist, **31**: 401–424.

Mposkos, E., and Wawrzenitz, N. 1995. Metapegmatites and pegmatites bracketing the time of HP-metamorphism in polymetamorphic rocks of the E-Rhodope, N. Greece: petrological and geochronological constraints. Bulletin of Geological Society of Greece, Special Publications, **4**(2): 602–608.

Mposkos, E., Perdikatsis, V., and Iliadis, A. 1994. Petrology of the metamorphic ultramafic rocks from the upper tectonic unit in East Rhodope: a contribution to the metamorphic evolution of the Rhodope zone. Bulletin of Geological Society of Greece, **XXX**(1): 241–254. [In Greek with English abstract.]

Mposkos, E., Baziotis, I., Palikari, S., Perraki, M., Krohe, A., and Hoinkes, G. 2004. Alpine UHP metamorphism in the Kimi complex of the Rhodope HP province N.E. Greece: mineralogical and textural indicators. *In* Proceedings of the 32rd International Geological Congress, Florence, Italy, 2004. Abstract Vol., Part 1, abstract 18-28, p. 108.

Okamoto, K., and Maruyama, S. 1998. Multi-anvil re-equilibration experiments of a Dabie Shan ultrahigh-pressure eclogite within the diamond-stability fields. Island Arc, **7**: 52–69.

O'Neill, H. 1981. The transition between spinel lherzolite and garnet lherzolite and its use as a geobarometer. Contributions to Mineralogy and Petrology, **77**: 185–194.

O'Neill, H., and Wood, B.J. 1979. An experimental study of Fe–Mg partitioning between garnet and olivine and its calibration as a geothermometer. Contributions to Mineralogy and Petrology, **70**: 59–70.

Ono, S. 1998. Stability limits of hydrous minerals in sediment and mid-ocean ridge basalt compositions. Implications for water transport in subduction zones. Journal of Geophysical Research – Solid Earth (B8), **13**: 18 252–18 267.

Perraki, M., Proyer, A., Mposkos, E., Kaindl, R., Baziotis, I., and Hoinkes, G. 2004. Micro- and nanodiamonds in garnets of metapelitic rocks from the Greek Rhodope: an in situ micro-Raman study. *In* Proceedings of the 5th International Symposium on Eastern Mediterranean Geology, Thessaloniki, Greece, 14–20 April 2004. pp. 1216–1219.

Perraki, M., Proyer, A., Mposkos, E., Kaindl, R., and Hoinkes, G. 2006. Raman micro-spectroscopy on diamond, graphite and other carbon polymorphs from the ultrahigh-pressure metamorphic Kimi Complex of the Rhodope Metamorphic Province, NE Greece. Earth and Planetary Science Letter, **241**: 672–685.

Ricou, L.E., Burg, J.P., Godfriaux, I., and Ivanov, Z. 1998. Rhodope and Vardar: the metamorphic and olistostromic paired belts related to Cretaceous subduction under Europe. Geodynamica Acta, **11**: 285–309.

Robertson, A.H.F., Dixon, J.E., Brown, S., Collins, A., Morris, A., Pickett, E. et al. 1996. Alternative tectonic models for the late Palaeozoic – early Tertiary development of Tethys in the Eastern Mediterranean region. *In* Palaeomagnetism and tectonics of the Mediterranean region. *Edited by* A. Morris and D.H. Tarlingeds. Geological Society (of London), Special Publication 105, pp. 239–263.

Rolfo, F., Compagnoni, R., and Wu, W.P. 2003. A coherent lithostratigraphic unit in the coesite-eclogite complex of Dabie Shan, China: Geologic and petrologic evidence. Lithos, **73**(1–2): 71–94.

Schmickler, B., Jacob, D.E., and Foley, S.F. 2004. Eclogite xenoliths from the Kuruman Kimberlites, South Africa: geochemical fingerprinting of deep subduction and cumulate processes. Lithos, **75**: 173–207.

Sokoutis, D., Brun, J.P., van den Driessche, J., and Pavlides, S. 1993. A major Oligo-Miocene detachment in the southern Rhodope controlling north Aegean extension. Journal of the Geological Society, London, **150**: 243–246.

Stamoudi, C., and Mposkos, E. 2005. Diamonds and Fe-carbonates inclusions in garnets from pelitic gneisses of the ultra-high pressure metamorphic Kimi complex in central and east Rhodope, Greece. *In* Proceedings of the 7th International Eclogite Conference, Seggau, Austria. Mitteilungen Gesellschaft Osterreichischer Geologiestudenten, 150, p. 149.

Stampfli, G.M., and Pillevuit, A. 1993. An alternative Permo Triassic reconstruction of the kinematics of the Tethyan realm. *In* Atlas Tethys, paleoenvironmental maps, explanatory notes. *Edited by* J. Dercourt, L.E. Ricou, and B. Vrielynck. Gaultier-Villards, Paris, France, pp. 55–62.

Stöckhert, B., Duyster, J., Trepmann, C., and Massonne, H.J. 2001. Microdiamond daughter crystals precipitated from supercritical COH + silicate fluids included in garnet, Erzgebirge, Germany. Geology, **29**: 391–394.

Storey, C.D., and Prior, D.J. 2005. Plastic deformation and recrystallization of garnet: a mechanism to facilitate diffusion creep. Journal of Petrology, **46**(12): 2593–2613.

Thompson, A.B. 1976. Mineral reactions in pelitic rocks: I prediction of $P–T–X$ (Fe–Mg) phase relations. America Journal of Science, **276**: 401–424.

Vielzeuff, D., and Holloway, J.R. 1988. Experimental determination of the fluid-absent melting relations in the pelitic system. Consequences for crustal differentiation. Contributions to Mineralogy and Petrology, **98**: 257–276.

Voegelé, V., Liu, B., Cordier, P., Wang, Z., Takei, H., Pan, P., and Karato, S. 1999. High temperature creep in a 2–3–4 garnet: $Ca_3Ga_2Ge_3O_{12}$. Journal of Materials Science, **34**(19): 4783–4791.

Wawrzenitz, N. 1997. Mikrostrukturell unterstützte Datierung von Deformationsinkrementen in Myloniten: Dauer der Exhumierung und Aufdomung des metamorphen Kernkkomplex der Insel Thasos (Südrhodope, Nordgriechenland). Doctoral thesis, University of Erlangen-Nürnberg, Erlangen, Germany.

Wawrzenitz, N., and Krohe, A. 1998. Exhumation and doming of

the Thasos metamorphic core complex (S. Rhodope, Greece): structural and geochronological constraints. Tectonophysics, **285**: 301–332.

Wawrzenitz, N., and Mposkos, E. 1997. First evidence for Lower Cretaceous HP/HT-metamorphism in the Eastern Rhodope, North Aegean Region, North-East Greece. European Journal of Mineralogy, **9**: 6589–6664.

Willner, A.P., Sebazungu, E., Gerya, T.V., Maresch, W.V., and Krohe, A. 2002. A numerical modelling of PT-paths related to rapid exhumation of high-pressure rocks from the crustal root in the Variscan Erzgebirge Dome (Saxony/Germany). Journal of Geodynamics, **33**(3): 281–314.

Yamoaka, S., Shaji Kumar, M.D., Kand, H., and Akaishi, M. 2002. Formation of diamond from $CaCO_3$ in a reduced C–O–H fluid at HP–HT. Diamond and Related Materials, **11**: 1496–1504.